Petrogenesis of South Armorican serpentinized peridotites

Geoffrey Aertgeerts, Jean-Pierre Lorand, Christophe Monnier, Carole La

Petrogenesis of South Armorican serpentinized peridotites

Geoffrey Aertgeerts[1,2], Jean Pierre Lorand[1*], Christophe Monnier[1] and Carole La[1]

1 : Laboratoire de Planétologie et Géodynamique à Nantes (LPG)

CNRS UMR6112, Université de Nantes, Faculté des Sciences et Techniques

2 Rue de la Houssinière - BP 92208 44322 NANTES CEDEX 3 - France

2 : Bureau de recherches géologiques et minières (BRGM).

DAT/OMR/GUY/CAY, B.P. 10552, 97333 Cayenne Cedex 2 - France

*: Corresponding author (jean-pierre.lorand@univ-nantes.fr)

Abstract Twenty three serpentinite samples collected from five outcrops in south Brittany (Audierne near Quimper, Champtoceaux near Nantes), western France, were studied using optical microscopy, electron microprobe (EMP), inductively-coupled optical emission spectroscopy (ICP-OES), inductively-coupled plasma mass spectrometry (ICP-MS), and laser ablation-inductively coupled plasma mass spectrometry (LA-ICPMS). Their bulk-rock major and trace element contents recomputed on an anhydrous basis are broadly characteristic of mantle-derived peridotites, as are the covariation trends of inert elements despite evidence of serpentinization-related remobilization of some fluid-mobile elements (FME; e.g., Ca, La, Ce, Sr, U). One outcrop near Champtoceaux shows fertile lherzolite compositions and chondrite-normalized rare earth element patterns consistent with low (5-7%) degree of mantle partial melting. The other four occurrences are harzburgites displaying higher partial melting degrees (15-25%). Regardless of their degree of fertility, our South Armorican peridotites bear evidence of high-temperature melt/fluid - rock metasomatic interaction yielding ~~to~~ an overall enrichment in highly incompatible elements (HIE; Cs, Rb, Ba, Th, U, Pb, La). Hydrous modal metasomatism has been identified in both lherzolites and harzburgites. The lherzolites reacted with HIE-enriched small-volume fluids at P = 1.5-2 Gpa for T >900°C that produced a Ti-poor pargasite. The Audierne harzburgites were pervasively refertilized by alkali-rich hydrous melts that precipitated K- and Cr-rich pargasite. Taken as a whole, South Armorican peridotites record a great diversity of protoliths, from supra-subduction zone ophiolites (Audierne) to arc-fore arc provenance.

I. Introduction

Serpentinized peridotites are widespread at plate boundaries, whether exposed in mid-ocean ridges, in collision zones or in transcurrent faults (Mével, 2003; Deschamp et al., 2013 and references therein). Serpentinized peridotites also crop out in the Armorican massif (western France) especially in the southern part of the massif that comprises the major suture zone between Gondwanian terranes and the Armorica microplate according to geodynamic models of the Variscan orogeny (Ballèvre et al., 2009, 2014; Faure et al., 2009 and references therein). This area from Brest to Nantes known as the South Armorican Domain shows a series of nappe-stacking complexes composed of high-pressure metamorphic rocks (eclogites; blue schists) and mafic/ultramafic rocks (amphibolites, metagabbros, peridotites), within metasedimentary/acid metamorphic rocks. Review papers on the Armorican massif interpreted these serpentinized peridotites as pieces of subducted and obducted oceanic lithosphere (the so-called Galice - Massif Central ocean) tectonically thrust along with remnants of continental margins during the early eo-Variscan event of the Variscan orogeny (Ballèvre et al. 2009; 2014; Faure et al., 2005, 2009). However, no detailed petrological study has ever been performed on these serpentinites that bear evidence of crustal deformation and locally strong weathering, in addition to being poorly exposed as discontinuous, small-~~sized~~ outcrops (Marchand et al., 1969, 1989; Béchennec et al., 1999; Aertgeerts et al., 2015). Their exact origin (mantle-derived tectonites or cumulate peridotites) thus remains unknown.

Our study focused on five occurrences of South Armorican (SA) peridotites from the Champtoceaux (near Nantes) and Audierne (80 km south of Brest, Finistère) nappe-stacking complexes. We performed a multiscale petrological study coupling thin section study by optical microscopy, electron microprobe analyses (EMPA), bulk-rock analyses of major and

trace elements by inductively-coupled plasma mass spectrometry (ICP-MS) and in-situ analyses of preserved minerals by laser ablation-ICPMS (LA-ICPMS). It is well known that geochemical signatures recorded in serpentinites are a complex combination of protolith partial melting, melt-rock interaction history, and serpentinization conditions (Deschamps et al., 2013; Cooperdock et al., 2018 and references therein). Some major elements (CaO, SiO_2, MgO), and light REE (LREE) can be mobilized during serpentinization and should be interpreted with caution (Paulick et al., 2006; Snow and Dick, 1995) while strong enrichment in fluid-mobile elements (FME; e.g., B, Li, Cl, As, Sb, Pb, U, Cs, Sr, Ba) may occur. All this secondary remobilization may alter the petrogenetic features of pre-serpentinization processes. Our first aim was therefore to unravel any potential alteration of protolith mineral assemblages by serpentinizing fluids. Our second goal was to provide tighter constraints on putative protolith compositions by identifying petrogenetic processes that typically occur in the upper mantle, such as partial melting events and fluid/melt-rock interactions (metasomatism).

2. Geological setting

The Armorican massif was structured into seven tectonometamorphic domains during the Variscan collision between Gondwanian terranes and the Armorica microplate (Ballèvre et al., 2009, 2014 and references therein). Each of these seven domains is separated from its neighbors by shear zones of regional extent that are interpreted as major suture zones (Fig. 1). The Champtoceaux Complex extends all over the northeastern area of Nantes, in the Nantes Variscan Domain (NVD) that is limited to the south by the South Armorican Shear Zone (SASZ) and to the north by the Nort-sur-Erdre fault (NEF) (Fig. 1A). The Champtoceaux

Complex is interpreted as a nappe-stacking structure thrust onto mica schists of late proterozoïc ages (Mauges Unit) during the early eo-Variscan event of the Variscan orogeny and subsequently twisted by the dextral movement of the SASZ (Ballèvre et al. 2014). From bottom to top, the Champtoceaux complex is composed of three structural units, a lower allochton, a middle allochton and an upper allochthnon, each one being separated by thrust faults (Fig. 1A). The lower allochthon unit consists of Ordovician orthogneisses (485 Ma; Paquette et al. 1984) enclosing eclogite lenses (Ballèvre et al. 2002) and garnet-chloritoid-chlorite-mica schists with high-pressure metasedimentary relicts (Pitra et al. 2010). Felsic rocks are thought to represent pieces from the northern margin of the Gondwana megacontinent (Ballèvre et al. 2009, 2014; Pitra et al. 2010). In more detail, the Cellier formation and Ordovician orthogneisses is overlain by garnet–staurolite–biotite micaschists of the Saint-Mars-du-Désert formation (Pitra et al. 2010). The middle allochthon unit is made up of amphibolites (Folie Siffait amphibolites). The upper allochthon (Champtoceaux formation) is an orthogneiss unit with eclogitic relics representing the southern margin of the Armorica microplate (Bosse et al. 2000; Ballèvre et al. 2009, 2014; Pitra et al. 2010). The Champtoceaux formation is overthrust by a younger (?) composite unit comprising the Drain formation (metagabbros of N-Type MORB affinity, mafic cumulates (Paquette et al., 1984) and serpentinites (Ballèvre et al. 2013)), the Le Hâvre formation (mica schists containing graphite-rich siliceous rocks known as “phtanites”) and Pont de Barel formation (Fig. 1A). This latter crops out in the northwestern part of the Champtoceaux complex, in tectonic contact with the le Hâvre micaschists.

The Audierne Complex is located in the westernmost part of the Armorican Massif, near Quimper, 80 km to the south of Brest, in the South Armorican Domain (Fig. 1B). It is

described in geological maps as a remnant of an ophiolitic complex, itself subdivided into the Audierne unit and the Trunvel-Tréogat unit (Plaine et al. 1981; Béchennec et al. 1999; Cagnard 2008). The northern part of the Audierne unit is composed of serpentinites (Ty-lan serpentinites) whereas the southern part consists of metagabbros and amphibolites (Peumerit formation) displaying N-MORB affinities (Bernard-Griffiths and Cornichet 1985; Béchennec et al. 1999). A few chromitite occurrences were recognized inside the Peumerit formation, but their field relationships with surrounding rocks are unknown (BRGM, «Mineralogical Inventory of Finistère», 1975). The Trunvel-Tréogat unit consists of amphibolites in its northern part (Tréogat formation) and mica schists in its southern part (Trunvel formation). To the north, the Trunvel-Treogat formation is overlain by the Penhors formation, the southernmost continental margin of the Armorica microplate according to Ballèvre et al. (2014).

3. Sampling

The 23 serpentinites studied were collected from Ty Lan outcrop in the Audierne complex (10 samples) and four outcrops throughout the Champtoceaux complex (Fig. 1A), i.e., Folies Siffait from the middle allochthon unit, Le Havre Fomation (l'Orgerais serpentinites), Pont-de-Barrel formation and Drain formation (Butte de la Roche) from the Champtoceaux unit. The Folies Siffait serpentinites were sampled in a 50 m^2 outcrop near the small town of Oudon along the Loire river bank (Fig. 1A). The Butte de la Roche serpentinites were sampled 10 kilometers eastward of the city of Nantes from occasional outcrops in the bank of the roads near La Haie-Fouassière. The l'Orgerais serpentinites were sampled in a small carry between Blain and Heric, not far from the tectonic contact with the late carboniferous pull-appart sedimentary basin of Ancenis (Fig. 1A). The Pont de Barel

serpentinites were sampled in an amphibolite quarry that exposes a 50-60 m^2 outcrop of peridotites near the small village of Saint Omer de Blain.

Thin sections and rock powders were done from the carbonate-free interiors of serpentinized blocks, previously cleaned up from any supergene alteration product. These serpentinite cores consist in pseudomorphic, retrogressive lizardite + magnetite + chrysotile assemblages (Aertgeerts et al, 2015). At Folie Siffait and L'Orgerais, this assemblage was partly overprinted by a high stress, low-temperature deformation that generated mylonitic to ultramylonitic microtextures. In addition to pseudomorphic serpentinization assemblages, all Champtoceaux and Ty Lan serpentinites display various generations of chrysotile, from ubiquitous crack-seal veins penetrating deeply into serpentinite blocks (e.g. Pont de Barel) to chrysotile fiber veins contemporaneous to the penetrative deformations in L'Orgerais serpentinites.

4. Analytical methods

Thin sections were studied with an optical polarizing microscope, using transmitted and reflected light. The few minerals predating serpentinization (olivine, Cr-spinel, pargasite, see below) were analyzed with a CAMECA SX-100 electron microprobe at the Service Microsonde Ouest of Brest University. The analytical conditions for silicates and oxides were: accelerating voltage 15 kV, sample current 20 nA, beam diameter 1 μm, 10s peak counting and 5s background counting on either side of the peaks. Elemental concentrations were determined using both natural and synthetic compounds. A complete data set is given in supplementary data (Table S1, S2 and S3)

Major elements were analysed with a iCAP-6300 Thermo inductively-coupled plasma

optical emission spectrometer (ICP-OES) at the "Laboratoire de Planétologie et Géodynamique" (LPG) in Nantes. Each sample was crushed and powdered in an agate ring mill. The amount of sample powder was typically 125 mg, which were placed into Savillex beakers along with 0.5 milliliters of distilled concentrated HNO_3 (65%) and 40 drops of distilled concentrated HF. Savillex beakers were left dissolving overnight at 110°C. After cooling, the solution was transferred into a 100 ml bottle along with with 5 g of external standard solution (Ge 80 ppm, Co 80 ppm). 20 g/l of boric acid was added to neutralize hydrofluoric acid and the solution was left for another 48 hours. Elemental concentrations were determined with international rock standards JP-1, BIR-1, WS-E, W-2, and PM-S as external calibration standards.

Trace elements were analysed with a VARIAN 820MS inductively-coupled plasma mass spectrometer (ICP-MS). Solutions were prepared by dissolving 125 mg of sample powder in clean Savillex™ beakers, using 0.5 ml of milliQ water, 0.5 ml of bi-distilled HNO_3 (65%), 14 drops of bi-distilled HF (40%) and 3 drops of distilled perchloric acid $HClO_4$ (70%). This mixture was left overnight on a hotplate at 130°C and then evaporated at 110°C for 5 hours and at 120°C for 4 hours. The residuum was dissolved by the same protocol and left on an hotplate at 130°C for 48 hours. Then 1 ml of bi-distilled HNO_3 (65%) was added and the solution left on a hotplate at 120°C for 72 hours. After evaporation at 130°C for 12 hours, the residuum was dissolved with 1 ml of bi-distilled HNO_3 (65 %) at 110°C for 5 hours. The solution was then transferred into a 250 ml bottle weighed on a balance along with 50 g of 5% HNO_3 internal standard solution (10 ppb Ge, 4ppb Rh-In-Tm-Bi) and then adjusted to 250 g by

adding Milli Q water. Internal standard solution was used to correct for linear drift and matrix effect.

Analyzed isotopes and operating parameters for the ICP-MS are given in Table S5 (supplementary data). Elemental concentrations were determined with three international rock standards UB-N, JP-1 and BIR-1. Limits of detection are given Table 1. Precision and accuracy of solution ICP-MS analyses of major and trace element concentrations at LPG were tested against two peridotite reference materials (UB-N and JP-1) analysed as unknown. Our results agree within recommended values at 1 sigma level (Table 1).

Because it was mostly preserved from serpentinization (see below), amphibole was analysed by laser ablation inductively coupled plasma mass spectrometry (LA-ICPMS) at LPGN. The samples were ablated and collected using a Photon Machine Analyte G2 pulsed 193-nm ArF Excimer laser coupled with a VARIAN 820 quadrupole ICPMS system. The Photon Machine laser is equipped with a dual volume sample cell that keeps the sample volume small. Laser sampling was performed in an Ar atmosphere with He–H_2 (ratio 15:1) as a carrier gas with homogeneous beam diameters (85-110 μm). ^{29}Si was used as internal standard and NIST SRM 612 glass as external standard with reference values from Jochum et al. (2011). An in-house secondary standard (gem quality diopside from Madagascar previously analysed via solution ICPMS and LA-ICPMS in a set of laboratories from abroad) was included as an unknown during the analytical runs to test accuracy and reproducibility of LPGN in-situ analyses (Table S6). Our values generally agree within 10% with working values except for Ba and Sr data which were not reproduced. By contrast, both elements were detected in significant amounts in our samples .

5. Mineralogy

Despite extensive serpentinization and secondary mylonitic deformation in L'Orgerais and Folies Sifait occurrences, pre-serpentinization rock textures and high-temperature minerals can be recognized as well as variations in the original mineralogy between each of the five peridotite outcrops studied here.

Ty Lan samples are spinel- and opx-bearing peridotite (harzburgites) showing an overall coarse-grained texture. Olivine porphyroclasts up to several mm across can be identified (Fig. 2A). Those preserved olivines show a few kink banding with well spaced subgrain boundaries indicating high-temperature recristallisation (Mercier and Nicolas, 1975). Cr-spinel occurs in-between or inside olivine grains as strongly euhedral, small-sized brownish grains (usually <200 μm across) sometimes showing octahedral cross-sections; larger, ameboidal spinels are almost lacking. Cr-spinel is systematically replaced by porous ferrit-chromite (reflected-light microscopy data) and always surrounded by a 100-200 μm-thick chlorite corona which may locally replace the spinel (e.g. TGA341 D). Orthopyroxenes (now totally replaced by Al-rich bastites) occur as very small ovoid grain within the olivine matrix. Ty Lan peridotites show 10-15 vol. % (visual estimate) of rounded, sometimes twinned crystals (up to 300 μm across) of colourless amphibole devoid of undulose extinction under cross-polariser transmitted light (Fig. 2A). This amphibole may form discontinuous layers inside olivine-rich lithologies or polycristalline amphibole networks resulting from the recrystallization of larger grains. No specific association with Cr-spinel has been observed. Another secondary amphibole (identified as tremolite by EMPA) may also be observed as truncated prismatic crystals.

Champtoceaux peridotites as a whole show pre-serpentinization mineralogy of harzburgites. The Pont-de-Barel samples are rich in small-sized bastites (<500 x 200 μm) characterized by convex-inward grain boundaries. Cr-spinel (3-5 vol.%, visual estimate) occurs as both ameboidal grains, up to 500 μm in maximum dimension, and rare smaller (200 μm across at best), subequant grains. Both Cr-spinel occurrences preserved greenish to brownish core surrounded by an opaque ferritchomite and/or magnetite rim (Fig. 2D). No clinopyroxene, nor olivine, was identified, even in the least altered sample (TGA007C). By contrast, Pont-de-Barel harzburgites are rich in colourless amphibole (up to 10 % by vol.) crystallized as large, undeformed, often euhedral, twinned or elongated crystals; amphibole-spinel-bastite clusters are common and amphibole preserving spinel inclusions or bastite cores have been observed (Fig. 2B,C).

At Butte de la Roche, harzburgites display common, small-sized bastitized orthopyroxene, often associated with ameboidal Cr-spinel. This latter may now be totally replaced by serpentinization-derived magnetite and chlorite. At l'Orgerais, due to the secondary mylonitic deformation, spinel harzburgites exhibit elongated bastites porphyroclasts (> 1 mm in maximum dimension) showing undulose extinction under crossed-polarizer transmitted light. Cr-spinel occurs as abundant large, reddish translucent ameboidal grains up to 500 μm in maximum dimensions (Fig. 2 E,F). Ferritchromite or magnetite overgrowths are not rare (reflected light microscopy data) but unaltered spinel cores were mostly preserved.

Despite secondary penetrative foliation, olivine relics are surprizingly common in Folie Siffait harzburgites (Fig. 2G). It is devoid of undulose extinction or kink banding. Restitic olivine grains may preserve the same orientation through lizardite mesh textures, suggesting a millimetric size for the original olivine grains. No preserved pyroxene was identified but

orthopyroxene bastites are common (Fig. 2H), Bastites are either globular grains, up to 500 μm in diameter, immersed in olivine matrix, or tabular crystals associated with relict magnetite and/or serpentinized olivine. Such associations, up to 2 mm in maximum dimensions are pervasively penetrated by lizardite. No ameboidal nor equant spinel can be identified, which may be due to the high amount of chlorite in this occurrence. Colourless, undeformed secondary amphibole crystals (identified as tremolite by EMPA) are widespread (up to 10-20% by vol.).

6. Mineral chemistry

6.1 Olivine

Olivine compositions range from Fo_{89} for Folie Siffait olivines to Fo_{90} for Ty Lan olivines. Both show high NiO contents (0.27 - 0.42 wt%), within the compositional range of mantle-derived peridotites (Table S1).

6.2 Cr-spinel

Pont de Barel Cr-spinels are Al-rich ($0.07 < Cr\# < 0.15$; Cr# = Cr/Cr+Al (atomic percentages)) while the L'Orgerais deep-red ameboidal Cr-spinels are Cr-rich (Cr# = 0.45-0.67), as are Butte de la Roche spinels (Cr# = 0.33-0.54; Fig. 3; Table S2). Their Mg# (Mg/Mg+Fe (atomic percentages)) decreases from 0.65-0.73 in PdB spinels to 0.48-0.54 for l'Orgerais spinels. This negative correlation between Cr# and Mg# has been widely documented in mantle peridotites as a whole (e.g. Arai, 1994; Niu, 1997; Hellebrandt et al., 2001; Pearson et al., 2014 and ref. therein). However, south Armorican peridotites show Fe-

265 enriched Cr-spinel compositions compared to abyssal peridotites. TiO_2 and trivalent iron contents are low (<0.1 wt.%; $Fe^{3+}/Fe^{3+}+Al^{3+}+ Cr^{3+}$= 0.01-0.05). L'Orgerais and Butte de la Roche spinels are poorer in NiO compared to PdB spinels (< 0.1 vs. 0.25-0.39 wt%).

6.3 Amphibole

Porphyroclastic colorless amphibole from Pont-de-Barel and Ty Lan peridotites are 270 low-Ti (Ti<0.1 at. p.f.u.), low-K (<0.12 at. p.f.u.) Cr-bearing magnesian pargasites (Mg number (100 x Mg/Mg+Fe (atomic percentages)) = 87-90) characterized by tetraedral Al predominating over octaedral Al ($1.6<Al^{IV}<1.8$ (atom per formula unit); $0.32<Al^{VI}<0.63$) and incompletely filled A sites (Table S3; Fig. 4). Both are slightly nickeliferous (NiO = 0.1 wt.%). Pont-de-Barel pargasites show higher extent of richteritic substitution ($^{B}Ca_{-1}{}^{AV}$ - $^{B}Na_{1}{}^{A}Na_{1}$) and 275 are Ti- and Al^{IV}- richer. Ty Lan pargasitic hornblende are K- and Cr-richer (Fig. 5).

7. Whole-rock geochemistry

7.1 Major Elements

Our south Armorican peridotites show L.O.I values (11.5-15 wt.%) close to the observed values for theoretical serpentine minerals (average of 12.38 wt.%.; Deschamps et al., 280 2013), in agreement with petrographic data. There is no correlation between L.O.I. and CaO contents, which rules out a significant contribution of carbonates (Table 1). Taken as a whole, the bulk-rock analyses correspond to peridotites in the SiO_2 /MgO vs. Al_2O_3 plot of Fig. 6A. Our peridotites plot well within the compositional field of abyssal peridotites ($0.01 < Al_2O_3/SiO_2 < 0.075$; $0.75 < MgO/SiO_2 < 1.05$; Niu, 2004). These rock produce a trend of 285 increasing MgO/SiO_2 and decreasing Al_2O_3/SiO_2 that parallels the terrestrial mantle array

produced by melting processes (Fig. 6B). Pont-de-Barel peridotites are clearly less depleted ($0.06<Al_2O_3/SiO_2<0.07$) compared to the four other harzburgitic outcrops studied. These latter plot inside the compositional field of serpentinised abyssal harzburgites whereas Pont de Barel peridotites are closer to UB-N, a serpentinized lherzolitic international rock standard.

In the FeO vs. MgO and CaO vs. MgO diagrams of Fig. 7, south Armorican peridotites also plot within the field of abyssal peridotites and their serpentinised analogs. Taken as a whole, they are variably enriched in FeO compared to the terrestrial mantle melting arrays (Fig. 7A). However, their Mg numbers (89-91) are consistent with a mantle-derived origin (Workman and Harte, 2005; Bodinier and Godard, 2014 and references therein). Two Butte de la Roche samples are clearly outliers in both plots of Fig. 7 because of their lower Mg numbers (84-87) compared to mantle values. This MgO depletion trend operates with increasing MgO. One sample (TGA018J) clearly falls out of the field of abyssal peridotites of Niu (2004) in both parts of Fig. 7, yet Deschamp et al., (2013) reported few FeO-rich abyssal serpentinites.

South Armorican peridotites span a large range of variation in the CaO vs. MgO plot of Fig. 7B. The Pont de Barel fertile samples along with one Ty Lan pargasite-rich sample (TGA346B) show the highest CaO contents. L'Orgerais harzburgites, and one Ty Lan Al_2O_3-poor harzburgite TGA343A are strongly Ca-depleted compared to the other samples.

7.2 Trace Elements

Transition element concentrations plot well within the published mantle arrays in Fig. 8. There is no clear correlation between Ni (or Co) and Al_2O_3 (Fig 8A,B). Variations in spinel modal contents and/or compositional variations in this mineral (including those resulting from transformation into ferrichromite) can account for some outliers in the Cr vs. Al_2O_3 plot of Fig.

8C. Incompatible transition metals (Ti, V, Sc) broadly correlate positively with Al_2O_3: the Butte de la Roche Fe-rich samples display coupled enrichment in Fe, Ti, V and Cr (Fig. 8D to F).

South Armorican peridotites show incompatible trace element (ITE = Rare Earth Elements - REE, large ion lithophile elements - LILE, and high field strength elements - HFSE) spreading over the whole concentration ranges reported for mantle-rock and their serpentinized analogs (Fig. 9, 10). The samples studied are variably depleted in heavy REE (HREE) compared to MORB mantle source estimates (Workman and Hart, 2005). This HREE depletion degree (2.0 to 0.015 x CI-chondrite) increases in parallel with the Al_2O_3 depletion, i.e. from Pont-de-Barel samples to Ty Lan, Folie Siffait and l'Orgerais harzburgites. Middle REE (MREE) and Light REE (LREE) contents do not follow such clear covariation trends with fertility. Pont de Barel and Ty Lan peridotites show high but variable LREE concentrations (La_N up to 6; N = CI-chondite normalized) compared to published data for mantle peridotites. Pont-de-Barel samples display nearly flat CI chondrite-normalized patterns with moderate LREE enrichments (La_N/Sm_N = 1.3-4.2) that have been reported mainly from weakly metasomatized continental orogenic lherzolites (Fabriès et al., 1991, 1998; Bodinier and Godard, 2004). Ty Lan peridotites show negatively trending CI-chondrite normalized patterns coupling strong LREE- and MREE-enrichments (La_N/Sm_N = 2.7-5.6; Sm_N/Yb_N = 1.3-5.9) with HREE depletion ($0.38<Yb_N<1.09$; Fig. 9). Such patterns have been documented only in very metasomatised continental orogenic peridotites (e.g. Caussou, Fabriès et al. 1991; Bodinier and Godard, 2014). Taken as a whole, La_N/Yb_N increases at decreasing HREE contents. The Folie Siffait harzburgites exhibit spoon-shaped REE patterns (La_N/Sm_N = 1.80; Yb_N =0.87) while V-shaped REE patterns characterize the l'Orgerais harzburgites (La/Sm_N = 4.4-6.3; Sm_N/Yb_N = 0.55). Such patterns were documented in many mantle-derived

harzburgites, whether orogenic, ophiolitic or abyssal harzburgites (Deschamp et al., 2013; Bodinier and Godard, 2014; Fig. 9). The most striking difference with abyssal harzburgites is the lack of positive Eu* anomalies. Note that the three Butte de la Roche Fe-rich harzburgites display abnormally high REE concentrations compared to their low bulk-rock Al_2O_3 contents (Yb_N = 1.5 x CI-chondrites; La_N/Sm_N = 1.5-2.02; Sm_N/Yb_N = 1-2.6; Fig 9). Yttrium, a proxy of HREE, is also significantly enriched compared to the other analyzed samples (Table 1).

In addition of being LREE-enriched, South Armorican peridotites are variably enriched in LILE, i.e. Cs (4-80 x PM), Rb (0.3-3 x PM); Ba (0.4-4 x PM), Th (0.1-2.2 x PM) and U (0.4-100 x PM), where PM = Primitive Mantle) (Fig. 10). Despite some variability within a single occurrence, U_N/Th_N increases from 1.8 in Pont-de-Barel samples to 2.2-6.5 in Ty Lan harzburgites, 3.7 for l'Orgerais harzburgites, 7-22 for Butte de la Roche harzburgites and 59 in Folie Siffait harzburgites (N = PM normalized). The same is also true for Sr, Ba and Pb that all produce positive anomalies in the PM-normalized extended patterns of Fig. 10, with however, some exceptions (e.g. Butte de la Roche for Pb; both negative and positive Sr anomalies in Pont-de-Barel peridotites). L'Orgerais harzburgites fall closer to the compositional field of mantle wedge serpentinites, or fore-arc serpentinised harzburgites (eg Izu-Bonin harzburgites) that combine extreme Ba, Rb, Cs, Pb and Sr enrichment with strong REE depletion (Deschamp et al., 2013; Bodinier et al., 2014). Pont de Barel and Ty Lan samples plot within the field of refertilized abyssal harzburgites in Fig. 10. Ty Lan peridotites show strong negative anomalies of all five HFSE's ($3.8<La_N/Nb_N<27$; $0.13<Ti_N/Gd_N<0.48$). The same is true for two Butte de la Roche harzburgites ($4<La_N/Nb_N<80$ and $0.11<Ti_N/Gd_N<0.58$) (Fig. 10) whereas the Pont-de-Barel peridotites are devoid of Ti, Zr and Hf negative anomalies.

8. In-situ analyses trace element analyses of pargasite.

In-situ LA-ICPMS analyses and EMP analyses of pargasite yield very similar Ti and Cr contents in the two amphibole-rich samples from Pont de Barel (TGA007C) and Ty-Lan (TGA346C). (Compare Table S3 and S4). Pargasite is enriched in ITE by a factor 10 compared to the corresponding bulk-rock analyses. Its composition is highly reproducible within a single thin section (relative standard deviation RSD < 10% for REE). Ty Lan pargasite exhibits LREE-enriched negatively-trending CI-chondrite normalized REE patterns ($1.6<La_N/Yb_N<4.2$; $4.9<Sm_N/Yb_N<7.1$; N = CI-chondrite) that faithfully reproduce the whole-rock pattern (Fig. 11A). Pont de Barel pargasite displays the same selective LREE enrichment over MREE and HREE as the whole-rock analyses ($2.3<La_N/Sm_N<3.5$; $0.59<Sm_N/Yb_N<0.67$). The mantle-normalized extended ITE patterns of pargasite also reproduce the whole-rock patterns quite well apart from a strong depletion in Cs, a lack of a positive U anomaly ($0.64<U_N/Th_N<1.27$), a lack of a Nb-Ta negative anomaly in Ty Lan pargasite, and weaker Cs and Sr enrichment ($1.7<Sr_N/Nd_N<2.4$) coupled with stronger positive Pb anomalies ($4.7<Pb_N/Pr_N<5.1$) for Pont-de-Barel pargasite.

9. Discussion

9.1 Low-Temperature Hydrothermal Alteration and Elemental Mobility.

South Armorican peridotites are mantle-derived peridotites. Their preserved relic mineralogy (magnesian olivine Fo_{89-91}), Cr-spinel compositional range from Al-rich to Cr-rich end-members, orthopyroxene replaced by bastite, pargasite), their bulk-rock major element concentrations, and their various trace element patterns are consistent with such an origin. Geochemical data suggest that the South Armorican peridotites have sampled a great diversity

of mantle-derived protoliths indicating a combination of different high-temperature processes. Due to our limited sampling and the high degree of alteration, inferences on the low-temperature mobility of major and trace elements should be made before addressing those high-T mantle processes. It is well known that some major elements and incompatible trace elements can be mobilized during low-temperature serpentinization or high-temperature melt-rock interaction and should be interpreted with caution (Coleman, 1967; Paulick et al., 2006; Snow and Dick, 1995; Deschamps et al., 2013). It has long been postulated that serpentinization/ocean floor alteration can modify MgO/SiO_2 (Mével, 2003; Niu, 2004; Frost and Beard, 2007; Ullrich et al., 2010; Harvey et al., 2014). In the Deschamps et al. compilation (2013) of Fig. 6, our serpentinites fall within the oceanic array defined by abyssal peridotites (Bodinier and Godard, 2014; Niu, 2004), which is parallel to the terrestrial array but with lower values in MgO/SiO_2. This worldwide difference between terrestrial array and oceanic array is explained by a loss of MgO during low-temperature seafloor weathering (Niu, 2004; Snow and Dick, 1995). Concerning our samples, there is no evidence for further MgO losses or SiO_2 gain of regional extent. Our samples preserved Mg numbers values (89-91) consistent with a mantle-derived origin, despite a slight FeO enrichment compared to the mantle array (Fig. 7A). Only the three Butte de la Roche samples show distinctly lower Mg number in the binary plots of Fig. 7A, with sample TGA018J off the compositional field of mantle peridotites as a whole. However, if pervasive MgO loss had occurred, it should result in a parallel increase in all of the other element concentrations when recalculated on an anhydrous basis. According to Fig. 7A, the low MgO of Butte de la Roche samples is balanced by an almost parallel increase in FeO (in addition to a few trace elements element contents, V, Ti, Cr, Sc and REE). This relationship seems to rule out a low temperature origin for this peculiar geochemical signature.

Past studies have documented systematic depletion in Ca during serpentinization (Coleman, 1967; Snow and Dick, 1995; Niu, 2004; Bach and Klein, 2008; Fabriès et al., 1998; Iyers et al., 2008; Austrheim and Prestwick, 2008). Calcium and silicon are interpreted as mobile elements in hot hydrothermal fluids because of clinopyroxene breakdown. L'Orgerais harzburgites, as well as one Ty Lan sample (TGA342A), show a strong depletion in CaO (Fig. 7B), with respect to Al_2O_3 ($0.01<CaO/Al_2O_3<0.06$) and to the Depleted MORB mantle (DMM) composition ($CaO/Al_2O_3 = 0.8$; Workman and Hart, 2005). Scandium is usually considered to be a proxy of Ca as it partitions into the same primary phases (cpx-opx) while being inert in hydrothermal processes (cf Orberger et al., 1995; Pearson et al., 2014 and ref. therein). L'Orgerais harzburgites fall in the mantle arrays in the Sc vs. Al_2O_3 plot of Fig. 8 and their very high Sc/CaO ratios (0.04-0.08 vs. 0.0004 for the DMM) clearly point to a secondary CaO loss. In contrast, Ty Lan and Pont de Barel peridotites preserved higher whole-rock CaO/Al_2O_3 (0.3-0.8) and much lower Sc/CaO (0.001-0.0008), closer to the range of DMM values. Both CaO and Sc in those amphibole-rich samples are mostly hosted in pargasite that predates serpentinization processes (Table S3 and S4). As a matter of fact, CaO positively correlates with Na_2O (not shown). The other south Armorican peridotites analysed (Butte de la Roche and Folie Siffait) display intermediate CaO/Al_2O_3 (0.13-0.19) and Sc/CaO (0.004-0.006); whether this trend is representative of serpentinization-related mobilization of CaO, or related to the depletion in CaO of protoliths is unclear as no primary Ca-rich minerals were preserved.

Among trace elements, fluid mobile elements (FME; e.g., B, Li, As, Sb, Pb, U, Cs, Sr, Ba, LREE) record chemical exchange between rock and fluid during serpentinization (Deschamps et al., 2013 and references therein). Our bulk-rock analyses bear evidence of strong U, Pb and Sr enrichments compared to DMM or PM compositions (Fig. 10), as is usual

for mantle-derived serpentinized peridotites compared to nominally anhydrous peridotites of similar compositions (Bodinier and Godard, 2014 and reference therein). Such anomalies are undoubtedly a secondary enrichment feature because they are observed in all five peridotite outcrops studied here, regardless of other trace element systematics (Fig. 12). The positive U anomaly of bulk-rock analyses is not reproduced by in-situ analyses of Ty-Lan pargasite while the Pont-de-Barel pargasite is devoid of the Sr anomaly carried by bulk-rock analyses (compare Fig. 9 and Fig. 11). One may infer that both elements are mainly hosted in serpentinized olivine and pyroxenes. Hydrothermal remobilisation may also add LREE to altered peridotites and this secondary addition can be seen through binary plots involving highly inert elements of similar incompatible behaviour such as Nb or Th (Paulick et al., 2006; Deschamps et al., 2013). The plots in Fig. 13 clearly show two Butte de la Roche and several Ty Lan samples with anomalously high La/Nb and Ce/Th ratios compared to mantle-derived peridotites, whether abyssal, ophiolitic or orogenic samples. Such ratios are perfectly reproduced by in-situ analyses of Ty Lan pargasites (Fig. 11), which suggest a primary, protolith-derived origin for the LREE enrichment in this occurrence. We do not have in-situ analysis for the Butte de la Roche samples that are totally serpentinized (L.O.I. up to 15 wt.%). However, their $La_N/Ce_N > 1$ (Fig. 9) may be evidence for a secondary origin.

Seawater is believed to carry U, Sr, LREE and Eu whereas slab-derived fluids produced during the dehydration of sediments and altered oceanic lithosphere in the subduction channel can contribute Cs, Sr, Rb, Li, and LREE to altered peridotites (Paulick et al., 2006; Janecky and Seifried, 1986; Niu, 2004; Deschamps et al., 2013). As shown above, our samples are devoid of Eu positive anomalies compared to serpentinized abyssal peridotites (Fig. 9) while showing strong enrichments in Cs, Rb and Li that are considered to concentrate in slab-derived fluids (Fig. 10; Fig. 12). The high Li, Cs and Ba contents in totally serpentinized Butte de la

Roche samples is noteworthy, as is their $La_N/Ce_N > 1$ (see above). However, a uniform, low-T origin for these enhanced concentrations of Cs, Rb, Ba and Li is unlikely because 1) there is no covariation with U, Sr and Pb 2) in-situ analyses reveal high concentrations of Cs, Rb, Ba and Li in Ty Lan and Pont de Barrel pargasite, reflecting the bulk-rock concentrations (Table S4 and Fig. 11). It is the pargasite modal abundance that produces the broadly positive correlations in binary plots of Fig 13 A, B, C and F.

9.2 Nature and origin of the protoliths

Serpentinization had indisputable but limited effects on the bulk-rock geochemistry of South Armorican peridotites: a widespread contamination in the FME U, Pb and/or Sr, in addition to local contamination in LREE (Butte de la Roche), and CaO loss (l'Orgerais, Ty Lan depleted sample TGA343A). Except for those elements, there is no evidence of widespread geochemical deviation from precursor mantle protolith, perhaps because serpentinization was of «rock-dominated type» in the Paulick et al (2006) classification scheme. Immobile elements like Al_2O_3, TiO_2, and HREE can provide reliable indications on protolith compositions (Orberger et al, 1995; Bodinier, 1988; Bodinier et al 1988; Fabriès et al. 1998; Ulrich et al., 2010). Alumina correlates negatively with MgO contents as expected for mantle-melting residues (Frey, 1985; Jacques and Green, 1980; Bodinier, 1988) (Fig. 14A). Ytterbium (and its proxy Y) positively correlates with Al_2O_3 (Fig. 14B). Except Pont-de-Barel peridotites, the south Armorican peridotites studied have bulk-rock compositions strongly depleted in major (Al_2O_3, TiO_2) and incompatible trace elements (Sc, V, HREE). Their primary mineralogy corresponds to harzburgites with undetermined but likely minor proportions of altered clinopyroxene (Fig. 6). For Pont-de-Barel samples, their whole-rock compositions (as well as their Al-rich spinel compositions) are more consistent with lherzolitic pre-serpentinization

modal compositions. The fact that no clinopyroxene was identified in thin sections may be explained by the fact that clinopyroxene alteration products are very difficult to identify under the microscope (Wicks and Whittaker, 1977; Wicks et al.,1977). However, because clinopyroxene (like pargasite) is much more resistant to serpentinization, we suggest that Pont de Barel clinopyroxene was replaced by pargasite before serpentinization (see below).

Variable degrees of partial melting inside the mantle can be inferred from the large range of bulk-rock and Cr spinel compositions. It is well known that Cr-spinel Cr # increases in parallel with the degree of partial melting (e.g. Dick and Bullen, 1984; Ellebrandt et al., 2001). Where preserved from hydrothermal alteration, this mineral provides melting degree estimates (F) increasing from 5-10% for Pont-de-Barel lherzolites to 15-25% for Butte de la Roche samples and 20-25% for l'Orgerais harzburgites (Fig. 3). These values are supported by the melting curves from low-P (0.5-1.5 Gpa) experiments (Jaques and Green, 1980; Bodinier, 1988) using a DMM-like mantle composition as the source (Workman and Hart, 2005) and a Rayleigh near-fractional partial melting model (Niu 1997; Seyler et al., 2004; Barth et al., 2008; Ullrich et al., 2010, Walter, 2014). The results constrain F, the degree of mantle melting, between 7 and 10% for Pont de Barel lherzolites, to around 20% for Butte de la Roche and Ty Lan harzburgites (except TGA343A) and 25% for l'Orgerais and Folie Siffait samples (Fig. 14). TGA343A is the most refractory sample from the Ty Lan occurrence (Ni = 2450 ppm; Table 1). Its strong depletion in Sc, Ti and V is consistent with complete consumption of cpx that occurs for 25% partial melting (Herzberg, 2004; Pearson et al., 2014 and ref. therein).

The three Butte de la Roche harzburgites plot significantly off the partial melting curve in the Yb vs. Al_2O_3 diagram in Fig. 14 B and their interpretation as residual peridotites is far from being supported. Their high HREE content coupled with low Mg-number (83-87) are not typical of refractory mantle peridotites, apart from the cm-thick finely interlayered peridotites

inside pyroxenite banding described in orogenic peridotite massifs (Bodinier et al., 1988; Bodinier and Godard, 2014 and reference therein). The Butte de la Roche harzburgites plot in an area where peridotite and websterites overlap in the SiO_2/MgO vs. Al_2O_3 diagram of Fig. 6B. Thus, there is possibility that the Butte de la Roche harzburgites incorporated pyroxenites or pyroxenes from former pyroxenites that were dispersed within the peridotites by crustal shearing deformation. Although these rocks are now totally serpentinized, the pyroxene contamination scheme may account for the coupled enrichment in trace transition elements (Sc, Cr, V, Ti, Zn) and HREE.

9.3 Cryptic metasomatism in l'Orgerais and Folie Siffait harzburgites.

Our sampling provides compelling evidence for a great diversity of metasomatic processes that partly obliterated the partial melting history or south Armorican peridotites. These processes operated under different physical conditions within each of the five outcrops studied. Hereafter, for the sake of the discussion, we will adopt a well-accepted terminology in mantle petrology (Menzies and Dupuy, 1991; Bodinier and Godard, 2014), in making distinction between cryptic (i.e. trace element enrichment without precipitation of new phases) and modal metasomatism (trace element enrichments + precipitation of new minerals).

L'Orgerais and Folie Siffait harzburgites show indisputable evidence of cryptic metasomatism, such as incompatible trace element enrichments (including LILE : Cs, Rb, Ba, Th, La, Ce) coupled with strong depletion in basalt-forming major elements. Their spoon-shaped to U-shaped primitive-mantle normalized patterns in Fig. 10 have now been reported on a worldwide basis for olivine-rich mantle rocks, whether orogenic harzburgites (e.g. Lherz, Pyrénées, France; Bodinier et al., 1988; Fabriès et al., 1998; Downes et al., 1991; Le Roux et

al., 2007; Ronda, Van der Vall and Bodinier, 1996), ophiolitic harzburgites (e.g. New Caledonia (Ullrich et al., 2010); Cuba (Proenza et al., 2000), Seram Ambon, Indonesia, (Monnier et al., 2003)), or fore-arc peridotite xenoliths (e.g. Izu Bonin, Mariana; Parkinson and Pearce, 1998). Basically, ophiolitic and fore-arc xenolithic harzburgites are widely thought to have formed from fluid-assisted second-stage melting of already depleted mantle in supra-subduction zone settings, followed by percolation of Incompatible trace element (ITE)-enriched small melt fractions (Duncan and Green, 1987; Orberger et al., 1995; Barth et al., 2008; Ullrich et al., 2010). Whether partial melting and hydrous melt percolation are closely linked or occured as discrete, separated events has been widely debated from unserpentinized peridotites (e.g., Bodinier and Godard, 2014). Reactive melt percolation models predict that ITE that do not enter major mantle minerals can be concentrated in evolved liquid after a certain duration of percolative reactive melt transport (Godard et al., 1995). Our limited and completely altered sampling does not allow us more speculation. However, it is worth noting that l'Orgerais harzburgites display very similar PM-normalized ITE patterns as Izu-Bonin Mariana fore-arc peridotite xenoliths (Fig. 10). Arc- or back-arc geotectonic settings are well suited for such fluid percolation because of inverted geothermal gradients existing inside the mantle wedges above subducted slabs (Navon and Stolper 1987; Takazawa et al. 2003; Bodinier and Godard 2014 and references therein).

9.4 Modal metasomatism in Pont-de-Barel lherzolites and Ty Lan harzburgites.

There is little doubt that rounded pargasite porphyroclasts preserving twin growths predate serpentinization and syn-emplacement deformation of Pont de Barel lherzolites and Ty Lan harzburgites. Pargasite requires high temperature (900°C, up to 1100°C, depending on its Ti content) to crystallize in ultramafic compositions (Helz, 1982). Its Na content is also a

complex function of P and T. Niida and Green (1999), Green (2015) and Fumagalli et al. (2009) collectively concluded that the richteritic substitution ($^{B}Ca_{-1}^{AV}$ - $^{B}Na_{1}^{A}Na_{1}$) correlates with pressure (see also Pirrar and Hermann, 2015). According to these experimental data, the Pont-de-Barel and Ty Lan pargasite crystallized within the lowest P range (1.5-2 GPa) of the pargasite stability field. Pont de Barel pargasites that are slightly enriched in Ti, Na and Si may have crystallized at slightly higher P and T compared to Ty Lan pargasites, although this shift in P and T conditions cannot be accurately determined.

Pargasitic amphiboles were reported from a wide range of mantle peridotites encompassing margin or OCT (Ocean Continent Transition zone) peridotites (Agrinier et al. 1993), orogenic peridotites (Fabriès et al., 1991, 1998; Ionov and Hoffman, 1995; Bodinier et al. 1990; Zanetti et al. 1996, Vanucci et al., 1995), transform faults (Brunelli and Seyler, 2010), as well as in ophiolites and arc-related peridotite xenoliths (McInnes et al., 2001; Grégoire et al., 2002, 2008; Coltorti et al., 2007; Ishimaru et Arai 2008 and reference therein). Pargasite in South Armorican peridotites shows HFSE systematics, especially Ti/Nb, and Zr/Nb ratios closer to those of pargasites from arc-related xenoliths compared to pargasite in continental mantle rocks (McInnes et al., 2001; Grégoire et al., 2002, 2008; Coltorti et al., 2007). Likewise, the high $Fe^{3+}/Fe^{3+}+Fe^{2+}$ ratio (0.5-1) of Ty Lan and Pont de Barel pargasite suggests crystallization from a highly oxidized medium as expected for subducted slab-derived hydrous fluids. Beyond these compositional similarities, trace element distribution patterns and thin section microtextures provide compelling evidence for two different pargasite precipitation processes in our South Armorican peridotites.

Compared to Ty Lan pargasite, Pont-de-Barel pargasite is richer in Ti and poorer in Cr, in agreement with its crystallization from a rather fertile lherzolitic protolith. As discussed in

8.2, such a protolith should have contained clinopyroxene (> 10 vol. %), which was not identified in our thin sections. Thus, Pont de Barel metasomatic pargasite could reasonably be interpreted as a replacement product of clinopyroxene. Experiments (e.g. Helz, 1982) and observations in nature suggest that pargasite can be produced in the lithospheric mantle through reaction between clinopyroxene, spinel and hydrous fluids (e.g. Nickel and Green, 1984; Fabriès et al., 1991). This reaction is supported by abundant relict inclusions of Al spinel inside Pont-de- Barel pargasite. Likewise, such a reaction between hydrous fluids and clinopyroxene can account for the bulk-rock CI chondrite-normalized REE patterns and the fact that pargasite is the major host of the incompatible trace element budget of Pont-de-Barel lherzolites (Fig. 11). These rocks show selective LREE enrichment coupled with nearly unfractionated MREE and HREE relative abundances similar to depleted MORB mantle (DMM) composition. It is well known that clinopyroxene is the major host for REE in unmetasomatized mantle lherzolites corresponding to the DMM composition (Bodinier and Godard, 2014 and references therein). By comparison with previous work on mantle lherzolites (Bodinier et al., 1988; Downes et al., 1991, Seyler et al, 2004; Bedini and Bodinier, 1999; Pearson et al., 2014), the hypothetical precursor clinopyroxene in Pont-de-Barel lherzolites may be assumed to have provided MREE, HREE along with Ti, Zr, and Hf contents as well as part of the transition element budget (Sc, V, and Ti). By reacting out, the clinopyroxene produced pargasite that inherited its lithophile trace element budget from both the residual clinopyroxene and the LILE- and LREE-enriched metasomatic fluid. The nearly constant bulk-rock Al_2O_3 contents suggest that this metasomatic reaction was isochemical for major elements, despite large variation in the elements preferentially partitioned into pargasite (e.g. Ti, Sc, Ba, Rb, Li, Sr; Table S4 and Figs 8; 12). If pargasite had been a primary

precipitate, its amount (up to 10 vol. % according to visual modal estimates on thin section) might have resulted in drastic changes in bulk-rock Al_2O_3 and CaO contents that are not observed in our sampling.

Unlike Pont de Barel pargasite, there are neither thin section data nor geochemical evidence suggesting a direct replacement of clinopyroxene by pargasite in Ty Lan harzburgites. Ty Lan pargasite may occur as clusters or aggregates of several crystals networking, suggesting that it was a primary precipitate from intergranular melt or fluids. Extensive melt percolation inside a refractory harzburgitic protolith may account for the Cr-rich composition of Ty-Lan pargasite and the low Mg number (90) of Ty Lan olivine compared with the inferred modal composition of host rock (c.f. Arai 1994; Orberger et al., 1995; Beard and Johnson, 2004). Finally, some elements entering pargasite ~~composition~~ (e.g. Sc, V, Sr) display positive correlations with Al_2O_3 (Fig. 8) that may be interpreted as refertilization trends. For instance the bulk-rock major element composition of TGA346AB, the most fertile and pargasite-rich Ty Lan harzburgite can be reproduced by adding 10 % pargasite to the most depleted harzburgite TGA343A.

Regarding the composition of this putative silicate melt that precipitated pargasite in Ty lan harzburgites, the very high LREE and MREE contents of Ty Lan pargasite have been documented only in highly metasomatised amphibole-rich orogenic peridotites that have reacted with alkali basalts (e.g. Caussou, Fabriès et al., 1989) or in Ti-rich pargasite collected in the vicinity of high-pressure cumulates from alkali basalt (Bodinier et al., 1990; Downes et al., 1991; Zanetti et al., 1996; Liu et al., 2010). An alkali melt composition is supported by the overall negatively trending CI-chondrite normalized REE patterns of Ty Lan harzburgites and its pargasite. However the strong HFSE depletion of Ty Lan samples is in disagreement with

orogenic Ti-rich amphibole. This observation points to the origin of this putative metasomatic alkali melt from supra-subduction mantle wedge.

10. Conclusions.

Our new data identify South Armorican peridotites as mantle-derived peridotites having experienced moderate alteration of their fluid mobile element inventory by serpentinization. Immobile major element concentrations and preserved primary minerals (e.g., Cr-spinel) point to very variable degrees of melt depletion. Pont de Barel lherzolites represent the most fertile end members. All four other occurrences are identified as harzburgites having experienced up to 25% partial melting. Such rocks at Ty Lan are consistent with geological mapping of an ophiolitic complex.

South Armorican peridotites bear evidence of a complex metasomatism history postdating partial melting. The most refractory l'Orgerais and Folie Siffait harzburgites show evidence of cryptic metasomatism, perhaps associated with secondary melting. High-temperature pargasite precipitation indicates hydrous modal metasomatism in both Pont de Barel lherzolites and Audierne harzburgites. This pargasite precipitated in Pont de Barel lherzolites by reaction of residual clinopyroxene with incompatible trace element-enriched small-volume fluids. It was a primary precipitate from alkali-rich hydrous melts that pervasively refertilized the Ty Lan harzburgites.

South Armorican peridotites are not easy to constrain in terms of geotectonic provenance. A large degree of freedom remains for Pont-de-Barel lherzolites, from continental mantle to ocean-continent transition or back-arc settings (Menzies and Dupuy, 1991; Bodinier

and Godard, 2014 and reference therein.). Bulk-rock major and trace element compositions of the other peridotite occurrences studied suggest an origin from a paleo-oceanic lithosphere, from abyssal to mantle wedges or fore-arc settings. Unlike abyssal peridotites, however, South Armorican harzburgites are devoid of positive Eu anomalies.

Mantle wedge serpentinites and arc peridotites show on average low bulk TiO_2 (and depleted HFSE contents), Fe-rich Cr-spinel, and large LILE enrichments (Arai, S., 1994; Arai et al., 2003; Grégoire et al., 2007; Bédard et al., 2009; Deschamps et al., 2013; Bodinier and Godard, 2014 and references therein), all three features that are reproduced by our South Armorican harzburgites. Melting degrees exceeding 20% are usually ascribed to supra-subduction settings, because slab-derived hydrous fluids lower melting temperatures (Duncan and Green, 1987; Orberger et al., 1995). The coupled occurrence of harzburgites and chromite as recorded by Ty Lan samples were also reported from supra-subduction zone ophiolites. Regardless of their ultimate origin, both lherzolites and harzburgites may display sign of interaction with oxidized slab-derived melt/fluids, as suggested by metasomatic pargasite displaying Li-, Cs-, Rb-, Ba- enriched and HFSE-depleted composition.

Acknowledgements.

This work was made possible thanks to a «Pays de la Loire-BRGM-Institut Carnot» joint grant to Geoffrey Aertgeerts. Financial funding for analytical work was provided by LPGNantes-CNRS. Jessica Langlade is thanked for her help during electron microprobe analyses, Laurent Lenta for the thin sections and Roger H. Hewins for having corrected the English. The authors are grateful to an anonymous reviewer and Elisabeta Rampone who greatly improved this

manuscript.

References

Aertgeerts, G., Lorand, J.-P., Monnier, C., La C., Lahondère, D., 2015. New petrological and geochemical constraint on amphibolites and serpentinised peridotites from the variscan Champtoceaux complex, south armorican Massif, France. The variscan belt: correlation and plate dynamics. Special meeting of the French and Spanish Geological societies. Géologie de la France and surrounding areas, N°1, p. 19, 2015.

Agrinier, P., Mével, C., Bosch, D., Javoy, M., 1993. Metasomatic hydrous fluids in amphibole peridotites from Zabargad Island (Red Sea). Earth and Planetary Science Letters 120, 187-205.

Arai, S., 1994. Characterization of spinel peridotites by olivine-spinel compositional relationships: Review and interpretation. Chemical Geology 113, 191–204.

Arai, S., Ishimaru, S., Okrugin, V.M., 2003. Metasomatized harzburgite xenoliths from Avacha volcano as fragments of mantle wedge of the Kamchatka arc : Implication for the metasomatic agent. The Island Arc 12, 233246.

Austrheim, H., Prestvik, T., 2008. Rodingitization and hydration of the oceanic lithosphere as developed in the Leka ophiolite, north-central Norway. Lithos 104, 177–198.

Bach, M., Klein, F., 2008. The petrology of seafloor rodingites: Insights from geochemical reaction path modeling. Lithos 112, 103-117.

Ballèvre, M., Bosse, V., Ducassou, C., Pitra, P., 2009. Palaeozoic history of the Armorican Massif: Models for the tectonic evolution of the suture zones. Comptes Rendus Geoscience 341, 174201.

Ballèvre, M., Bosse, V., Dabard, M., Ducassou, C., Fourcade, S., Paquette, J., Peucat, J., Pitra, P., 2013. Histoire géologique du Massif armoricain : actualité de la recherche, 596.

Ballèvre, M., Capdevila, R., Guerrot, C., Peucat, J.-J., 2002. Discovery of an alkaline orthogneiss in the eclogite-bearing Cellier Unit (Champtoceaux Complex, Armorican Massif): a new witness of the Ordovician rifting. Comptes Rendus Geoscience, 334, 303311.

Ballèvre, M., Martinez Catalan, J.R., Lopez-Carmona, A., Pitra, P., Abati, J., Fernandez, R.D., Ducassou, C., Arenas, R., Bosse, V., Castineiras, P., (2014) Correlation of the nappe stack in the Ibero-Armorican arc across the Bay of Biscay: a joint French-Spanish project. Geological Society, London, Special Publications, 77-113.

Barth, M.G., Mason, P.R.D., Davies, G.R., Drury, M.R., 2008. The Othris Ophiolite, Greece: a snapshot of subduction initiation at a mid-ocean ridge. Lithos 100 (1–4), 234–254.

Beard, B.L., Johnson, C.M., 2004. Inter-mineral Fe isotopic variations in mantle-derived rocks and implications for the Fe geochemical cycle. Geochimica et Cosmochimica Acta 68: 4727–4743.

Béchennec, F., 2007. Carte géologique harmonisée du département de Loire-Atlantique BRGM/RP-55703-FR.

Béchennec, F., Hallégouët, B., Thiéblemont, D., Guerrot, C., Cocherie, A., Carn, A., 1999. Notice explicative, Carte géol. France (1/50 000), feuille de Quimper (346). Orléans BRGM. Géological map by Béchennec et al. (1999), 160 pp.

Bédard, É., Hébert, R., Guilmette, C., Lesage, G., Wang, C.S., et Dostal, J. 2009. Petrology and geochemistry of the Saga and Sangsang ophiolitic massifs, Yarlung Zangbo Suture Zone, Southern Tibet: Evidence for an arc-back-arc origin. Lithos 113, 48−67.

Bernard-Griffiths, J., Cornichet, J., 1985. Origin of eclogites from South Brittany, France: A Sm-Nd isotopic and REE study. Chemical Geology 52, 185-201.

Bodinier, J.-L., 1988. Geochemistry and petrogenesis of the Lanzo peridotite body, Western Alps. Tectonophysics 149, 67–88.

Bodinier, J.-L., Dupuy, C., Dostal, C., 1988. Geochemistry and petrogenesis of Eastern Pyrenean peridotites. Geochimica et Cosmochimica Acta 52, 2893–2907.

Bodinier, J.L., and Godard, M. (2014) Orogenic, Ophiolitic, and Abyssal Peridotites, 3e éd., vol 3-4 pp. 103-167. Treatise on Geochemistry: Second Edition Vol. 3. Elsevier Ltd.

Bodinier, J.L., Vasseur, G., Vernières, J., Dupuy, C., Fabries, J., 1990. Mechanisms of Mantle Metasomatism: Geochemical Evidence from the Lherz Peridotite. Journal of Petrology 31, 597628.

Bosse, V., Feraud, G., Ruffet, G., Balle, M., 2000. Late Devonian subduction and early-orogenic exhumation of eclogite-facies rocks from the Champtoceaux Complex (Variscan belt , France), 325, 297-325.

Brunelli, D., Seyler, M., 2010. Asthenospheric percolation of alkaline melts beneath the St. Paul region (Central Atlantic Ocean). Earth and Planetary Science Letters 289: 393–405.

Cagnard, F., 2008. Carte géologique harmonisée du département du Finistère notice géologique - BRGM/RP- 56273 - FR.

Canil, D., 2002. Vanadium in peridotites, mantle redox and tectonic environments: Archean to present. Earth and Planetary Science Letters 195, 75–90.

Chazot, G, Menzies, M.A., Harte, B., 1996. Determination of partition coefficients between apatite, clinopyroxene, amphibole and melt in natural spinel lherzolites from Yemen: Implications for wet melting of the lithospheric mantle. Geochimica et Cosmochimica Acta 60, 423–437.

Cooperdock, E.G., Raia, N.H., Barnes, J.D., Stockli, D.F., Schwarzenbach, E.M. (2018) Tectonic origin of serpentinites on Syros, Greece: Geochemical signatures of abyssal origin preserved in a HP/LT subduction complex. Lithos 296–299, 352–364

Coleman, R. G., Keith, T. E., 1971. A chemical study of serpentinization—Burro Mountain. California. Journal of Petrology 12, 311–329.

Coltorti, M., Bonadiman, C., Faccini, B., Grégoire, M., O'Reilly, S.Y., Powell, W., 2007. Amphibole from suprasubduction and intraplate lithospheric mantle. Lithos 99, 68-84.

Deschamps, F., Godard, M., Guillot, S., Hattori, K., 2013. Geochemistry of subduction zone serpentinites: A review. Lithos 178, 96127.

Dick, H.J.B., Bullen, T., 1984. Chromian spinel as a petrogenetic indicator in abyssal and alpine-type peridotites and spatially associated lavas. Contributions to Mineralogy and Petrology 86, 54–76.

Downes H, Bodinier J-L, Thirlwall MF, Lorand J-P, and Fabries J (1991) REE and Sr–Nd isotopic geochemistry of the Eastern Pyrenean peridotite massifs: Sub-continental lithospheric mantle modified by continental magmatism. Orogenic Lherzolites and Mantle Processes. Journal of Petrology Special Volume, 97–115.

Duncan, R.A., Green, D.H., 1987. The genesis of refractory melts in the formation of oceanic crust. Contribution to Mineralogy and Petrology 96, 326-342.

Fabriès, J., Bodinier, J.-L., Dupuy, C., Lorand, J.-P., and Benkerrou, C. (1989) Evidence for modal metasomatism in the orogenic spinel lherzolite body from Caussou (Northeastern Pyrénées, France). Journal of Petrology 30, 199–228.

Fabriès, J., Lorand, J.-P., Bodinier, J.-L., 1998. Petrogenetic evolution of orogenic lherzolite massifs. Tectonophysics 292, 145-167.

Fabriès, J., Lorand, J.-P., Bodinier, J.-L., and Dupuy, C. (1991) Evolution of the upper mantle beneath the Pyrenees: Evidence from orogenic spinel lherzolite massifs. Orogenic Lherzolites and Mantle Processes. Journal of Petrology Special Volume 55–76.

Faure, M., Mézème, E.B., Cocherie, A., Rossi, P., Chemenda, A., Boutelier, D. (2008) Devonian geodynamic evolution the Variscan Belt, insights from the French Massif Central and Massif Armoricain. Tectonics 27, 119.

765

Faure, M., Lardeaux, J.-M., Ledru, P. (2009) A review of the pre-Permian geology of the Variscan French Massif Central. Comptes Rendus Geoscience 341, 202213.

Frey, F.A., Suen, C.J., and Stockman, H.W. (1985) The Ronda high temperature peridotite:
770 Geochemistry and petrogenesis. Geochimica et Cosmochimica Acta 49, 2469–2491.

Frost, B., R. and Beard, J., S., 2007. On silica activity and serpentinization. Journal of Petrology, 48, 1351-1368.

Godard, M., Bodinier, J.-L., Vasseur, G., 1995. Effects of mineralogical reactions on trace
775 element redistributions in mantle rocks during percolation processes: a chromatographic approach. Earth Planetary Science Letters 133, 449–461.

Green, D.H., 2015. Experimental petrology of peridotites, including effects of water and carbon on melting in the Earth's upper mantle. Physics and Chemistry of Minerals 42,
780 95122.

Grégoire M., Bell, D.R., Le Roex, A.P., 2002. Trace element geochemistry of phlogopite-rich mafic mantle xenoliths: theirclassification and their relationship to phlogopite-bearing peridotites and kimberlites revisited. Contributions to Mineralogy and Petrology 142, 603–625.

785

Grégoire, M., Jego, S., Maury, R.C., Polvé, M., Payot, B., Tamayo R.A.Jr., Yumul, G.P. Jr., 2008. Metasomatic interactions between slab-derived melts and depleted mantle: Insights from xenoliths within Monglo adakite (Luzon arc, Philippines). Lithos 103, 415-430.

Harvey, J., Savov, I.P., Agostini, S., Cliff, R.A., Walshaw, R., 2014. Si-metasomatism in serpentinized peridotite : The effects of talc-alteration on strontium and boron isotopes in abyssal serpentinites from Hole 1268a, ODP Leg 209. Geochimica et Cosmochimica Acta 126, 3048.

Hawthorne, F.C., Oberti, R., Harlow, G.E., Maresch, W. V., Martin, R.F., Schumacher, J.C., Welch, M.D., 2012. Ima report: Nomenclature of the amphibole supergroup. American Mineralogist 97, 20312048.

Hellebrand, E., Snow, J.E., Dick, H.J.B., Hofmann, A.W., 2001. Coupled major and trace elements as indicators of the extent of melting in mid-ocean-ridge peridotites. Nature 410, 677–681.

Helz, R.T., 1982. Experimental studies on amphibole stabilities. Review in Mineralogy 12, 279-346.

Herzberg, C.T. , 2004. Geodynamic Information in Peridotite Petrology. Journal of Petrology 45, 1-24.

Ionov, D. A., Hofmann, A. W., 1995. Nb–Ta–rich mantle amphiboles and micas: implications for subduction-related metasomatic trace element fractionations. Earth Planetary Science

Letters 131, 341–356.

Ishimaru, S., Arai, S., 2008. Calcic amphiboles in peridotite xenoliths from Avacha volcano, Kamchatka, and their implications for metasomatic conditions in the mantle wedge. Geological Society, London, Special Publications 293, 3555.

Jaques, A.L., Green, D.H.,1980. Anhydrous melting of peridotite at 0–15Kb pressure and the genesis of tholeiitic basalts. Contributions to Mineralogy and Petrology 73, 287–310.

Janecky, D.R., Seyfried Jr., W.E., 1986. Hydrothermal serpentinization of peridotite. Geochimica et Cosmochimica Acta 48, 1351–1368.

Jochum K.P., Weis U., Stoll B., Kuzmin D., Yang Q., Raczek I., Jacob D.E., Stracke A., Birbaum K., Frick D.A., Günther D., Enzweiler J., 2001. Determination of Reference Values for NIST 610-617 Glasses Following ISO Guidelines. Geostandard and Geoanalytical Research 35(4), 397-429.

Le Roux, V., Bodinier, J.-L., Tommasi, A., et al., 2007. The Lherz spinel lherzolite: Refertilized rather than pristine mantle. Earth and Planetary Science Letters 259, 599–612.

Liu, C.Z., Wu, F.Y., Wilde, S. A., Yu, L.J., Li, J.L., 2010. Anorthitic plagioclase and pargasitic amphibole in mantle peridotites from the Yungbwa ophiolite (southwestern Tibetan Plateau) formed by hydrous melt metasomatism. Lithos 114, 413422.

Locock, A.J., 2014. An Excel spreadsheet to classify chemical analyses of amphiboles following the IMA 2012 recommendations. Computers and Geosciences 62, 111.

Lorand, J.-P., Ceuleneer, G., 1989. Silicate and base-metal sulfide inclusions in chromites from the Maqsad area (Oman ophiolite) : a model for entrapment. Lithos 22, 173-191.

Marchand, J., Perrin, J., Weeksteen, G., Forestier, F.H., Lasnier B., 1969. Notice explicative, Carte géol. France (1/50 000), feuille de Vallet (482). Orléans BRGM. Geological map by Marchand et al. (1969).

Marchand, J., Sellier, D., Alix, Y., Etienne, H., Lulzac, Y., 1989. Notice explicative, Carte géol. France (1/50 000), feuille de Savenay (450). Orléans BRGM. Geological map by Marchand et al. (1989).

McDonough, W. F., Sun, S. S., 1995. The composition of the earth. Chemical Geology 120, 223–253.

Mcinnes, B.I.A., Grégoire, M., Binns, R.A., Herzig, P.M., Hannington, M.D., 2001. Hydrous metasomatism of oceanic sub-arc mantle, Lihir, Papua New Guinea : petrology and geochemistry of fluid-metasomatised mantle wedge xenoliths. Earth and Planetary Science Letters 188, 169-183.

McPherson, E., Thirlwall, M.F., Parkinson, I.J., Menzies, M.A., Bodinier, J.-L., Woodland, A., and Bussod, G., 1996. Geochemistry of metasomatism adjacent to amphibole-bearing veins in the Lherz peridotite massif. Chemical Geology134, 135157.

Menzies, M.A., Dupuy, C., 1991. Orogenic massifs: Protolith, process and provenance. Orogenic Lherzolites and Mantle Processes. Journal of Petrology Special Volume, 1–16.

Mercier, J.-C.C., Nicolas, A., 1975. Textures and fabrics of upper-mantle peridotites as illustrated by xenoliths from basalts. Journal of Petrology 16, 454–487.

Mével, C., 2003. Serpentinization of abyssal peridotites at mid-ocean ridges. Comptes Rendus Geoscience 335, 825852.

Monnier, C., Girardeau, J., Permana, H., Rehault, J.-P., Bellon, H., Cotten, J., 2003. Dynamics and age of formation of the Seram-Ambon ophiolites (Central Indonesia). Bulletin de la Sociéte Géologique de France 174, 529-543.

Navon, O., Stolper, E., 1987. Geochemical consequences of melt percolation: the upper mantle as chromatographic column. The Journal of Geology 95, 285307.

Nickel, K. G., Green, D. H., 1984 The nature of the upper-most mantle beneath Victoria, Australia as deduced from ultramafic xenoliths. Developments in Petrology (11B) Kimberlites, Vol. 2, pp. 161-178.

Niida, K., Green, D.H., 1999. Stability and chemical composition of pargasitic amphibole in MORB pyrolite under upper mantle conditions. Contributions to Mineralogy and Petrology 135, 1840.

Niu, Y., 1997. Mantle melting and melt extraction processes beneath ocean ridges: Evidence from abyssal peridotites. Journal of Petrology 38, 1047–1074.

Niu, Y., 2004. Bulk-rock major and trace element compositions of abyssal peridotites: implications for mantle melting, melt extraction and post-melting processes beneath mid-ocean ridges. Journal of Petrology 45, 2423–2458.

Orberger, B., Lorand J.-P., Girardeau, J., Mercier, J.C.C., Pitragool S., 1995. Petrogenesis of ultramafic rocks and associated chromitites in the Nan-Uttaradit ophiolite, Northern Thailand, Lithos 35, 153-182.

Parkinson, I.J., Pearce, J.A., 1998. Peridotites from the Izu-Bonin- Mariana Forearc (ODP Leg 125): evidence for mantle melting and melt–mantle interaction in a supra-subduction zone setting. Journal of Petrology 39, 1577–1618.

Paquette, J.-L., Peucat, J.-J., Bernard-Griffiths, J., Marchand, J., 1985. Evidence for old Precambrian relics shown by U-Pd zircon dating of eclogites and associated rocks in the Hercynian belt of South Brittany, France. Chemical Geology 52, 203216.

Paulick, H., Bach, W., Godard, M., Hoog, C.-J., Suhr, G, Harvey, J., 2006. Geochemistry of abyssal peridotites (Mid-Atlantic Ridge, 1520'N, ODP Leg 209): Implications for fluid/rock interaction in slow spreading environments. Chemical Geology 234, 179–210.

Pearson, D.G., Canil, D. Shirey, S.B., 2014. Mantle Samples Included in Volcanic Rocks: Xenoliths and Diamonds Holland HD and Turekian KK (eds.) Treatise on Geochemistry. 2nd edition. In: Carlson RW (ed.) Oxford: Elsevier-Pergamon. The Mantle and Core, vol. 3-5, pp. 170-229.

Peters, D., Pettke, T. 2017. Evaluation of Major to Ultra Trace Element Bulk Rock Chemical Analysis of Nanoparticulate Pressed Powder Pellets by LA-ICP-MS. Geostandards and Geoanalytical Research, 41, 5-28.

Pitra, P., Ballèvre, M., Ruffet, G., 2010. Inverted metamorphic field gradient towards a Variscan suture zone (Champtoceaux Complex, Armorican Massif, France). Journal of Metamorphic Geology 28, 183208.

Plaine, J., Peucat, J.-J., Morzadec-Kerfourn, M.-T., Pinot, J.-P. 1981. Notice explicative, Carte géol. France (1/50 000), feuille de Pont-Croix (345). Orléans BRGM. Geological map by Plaine et al. (1981), 48.

Proenza, J., Gervilla, F., Melgarejo, J.-C., Bodinier, J.-L., 1999. Al-rich and Cr-rich chromitites from the Mayari-Baracoa ophiolitic belt (Eastern Cuba) as the consequence of interaction between volatile-rich melts and peridotites in suprasubduction mantle. Economic Geology 94, 547–566.

Seyler, M., Lorand, J.-P., Toplis, M.J., Godard, G., 2004. Asthenospheric metasomatism beneath the mid-ocean ridge; evidence from depleted abyssal peridotites. Geology 32, 301–304.

Snow, J. E., Dick, H. J. B., 1995. Pervasive magnesium loss by marine weathering of peridotite. Geochimica Cosmochimica Acta 59, 4219–4235.

Takazawa, E., Okayasu, T., Satoh, K., 2003. Geochemistry and origin of the basal lherzolites

from the northern Oman ophiolite (northern Fizh block). Geochemistry, Geophysics, Geosystems, 4.2000GC000080.

Ulrich, M., Picard, C., Guillot, S., Chauvel, C., Cluzel, D., Meffre, S., 2010. Lithos Multiple melting stages and refertilization as indicators for ridge to subduction formation : The New Caledonia ophiolite. Lithos 115, 223236.

Walter, M.J. , 2014. Melt Extraction and Compositional Variability in Mantle Lithosphere Holland HD and Turekian KK (eds.) Treatise on Geochemistry. 2nd edition. In: Carlson RW (ed.) The Mantle and Core, vol. 2, Oxford: Elsevier-Pergamon., 393-415.

Wicks, F.J., Whittaker, E.J.W., 1977. Serpentinite texture and serpentinization. Canadian Mineralogist 15, 459-488.

Wicks, F.J., Whittaker, E.J.W., Zussman, J., 1977. Model for serpentine textures after olivine. Canadian Mineralogist 15, 446-458.

Workman, R.K., Hart, S.R., 2005. Major and trace element composition of the depleted MORB mantle (DMM). Earth Planetary Science Letters 231, 53–72.

Zanetti, A., Vannucci, R., Bottazzi, P., Oberti, R., Ottolini, L., 1996. Infiltration metasomatism at Lherz as monitored by systematic ion-microprobe investigations close to a hornblendite vein. Chemical Geology 134, 113-133.

Figure captions

Figure 1 Location and schematic geological maps of Champtoceaux (A) and Audierne (B)

nappe stacking complexes (adaptated after Ballèvre et al., 2009, 2014 and references therein).

Figure 2 Microphotographs of thin sections of South Armorican peridotites. A : amphibole (pargasite)-olivine cluster in Ty Lan mesh-textured partly serpentinized harzburgite, crossed polariser transmitted light; B : pargasite porphyroclasts in Pont-de-Barel peridotites, crossed polariser transmitted light; C : pargasite porphyroclasts in partly serpentinized Pont de Barel, crossed polariser transmitted light; D : green-brown Cr-spinel associated with pargasite in Pont-de-Barel peridotites, plane polariser transmitted light; E :Cr-spinel isolated in l'Orgerais mylonitized harzburgite, plane polariser transmitted light; F : dark red anhedral spinel in l'Orgerais harzburgite; plane polariser transmitted light. G: olivine relics inside lizardite networks in Folies Siffait harzburgite, crossed polariser transmitted light; H : highly deformed opx bastite in Folie Siffait harzburgite, plane polariser transmitted light; Amp : amphibole; Ol : olivine; Spl : spinel; Srp : serpentine; Mesh Lz : mesh lizardite; Lz : lizardite; Atg : antigorite; Mag : magnetite.

Figure 3 Cr# vs. Mg# binary plot for Cr-spinel. Partial melting degrees (in percent) are from the Hellebrandt et al. (2001) calibration. Compositional fields for abyssal and fore-arc peridotites are from Bédard et al. (2009).

Figure 4 Pargasite compositions in a AlIV vs. Na+K diagram. Ed : edenite ; Hb : hornblende ; Pa : pargasite ; Ts : Tschermakite. Amphibole compositions were treated according to the IMA (International Mineralogical Association) recommendations (Hawthorne et al. 2012) and their structural formulae were calculated with the Excel spreadsheet of Locock (2014). Shaded field: compositional range of chromitite-hosted pargasite inclusions (Lorand and Ceuleneer, 1989).

Figure 5 Ti vs. Cr and Ti vs. K diagram for pargasite (at.%). Compositional field of continental peridotites from Fabriès et al. (1991).

Figure 6 A : Plot of South Armorican peridotite bulk-rock analyses (diamonds) in the MgO/SiO_2 vs. Al_2O_3 diagram of Bodinier and Godard (2014). B Plot of South Armorican peridotite bulk-rock analyses in the MgO/SiO_2 vs. Al_2O_3/SiO_2 diagram of Deschamp et al. (2013). Depleted Mantle after Workman and Hart (2005); Primitive mantle after McDonough and Sun (1995). Terrestrial array after Bodinier and Godard (2014). Compositional fields for abyssal serpentinites, mantle wedge serpentinites and subduction zone serpentinites after Deschamps et al. (2013).

Figure 7 FeO vs. MgO and CaO vs. MgO plots for bulk-rock analyses of south Armorican peridotites (anhydrous basis). Literature data: same references as in Fig. 6. Fig. 7A is contoured with iso Mg number lines (after Deschamp et al., 2013). Depleted Mantle after Workman and Hart (2005).

Figure 8 Binary diagrams of transition elements vs. Al_2O_3. Compositional fields for mantle peridotites after Bodinier and Godard (2014); Stars = Depleted mantle compositions (McDonough and Sun, 1995; Workman and Hart, 2005).

Figure 9 Chondrite-normalized bulk-rock Rare Earth Element concentrations. Chondritic values after McDonough and Sun (1995). Compositional fields for serpentinites after Deschamps et al. (2013). Those fields labelled “melt/rock interactions” correspond to samples that have been metasomatized within the upper mantle.

Figure 10 Extended primitive mantle-normalized bulk-rock concentrations of incompatible trace elements (ITE = Large Ion Lithophile Elements and Rare Earth Elements). Primitive mantle values after Mc Donough and Sun (1995). Compositional fields for serpentinites after

Deschamps et al. (2013). Those field labelled “melt/rock interactions” correspond to samples that have been metasomatized within the upper mantle. Compositions of ophiolitic, fast-spreading ridge harzburgites and arc-related harzburgites from Bodinier and Godard (2014).

Figure 11 (A) chondrite-normalized Rare Earth Element concentrations of pargasite; (B) Primitive Mantle-normalized incompatible trace element (ITE) concentrations of pargasite Normalizing values from Mc Donough and Sun (1995).

Figure 12 Binary plots of Large Ion Lithophile trace elements vs Al_2O_3. DMM composition after Workman and Hart (2005).

Figure 13 Plots of Incompatible Trace Elements in Nb vs. La and Th vs. Ce binary diagrams (bulk-rock analyses). Arrows relating to fluid-rock and melt-rock interactions are from Paulick et al. (2006). Compositional field for abyssal peridotites from Paulick et al. (2006), Deschamp et al. (2013). Orogenic and ophiolitic peridotites from Bodinier and Godard (2014).

Figure 14 Estimate of partial melting degrees from low-P experiments (Jaques and Green, 1980) or melting models (Bodinier, 1988; Herzberg, 2004); DMM mantle source from Workman and Hart (2005). The compositional fields of fore-arc peridotites are from Ullrich et al. (2010) and Bodinier and Godard (2014) for orogenic, ophiolitic and abyssal peridotites.

Figure 1

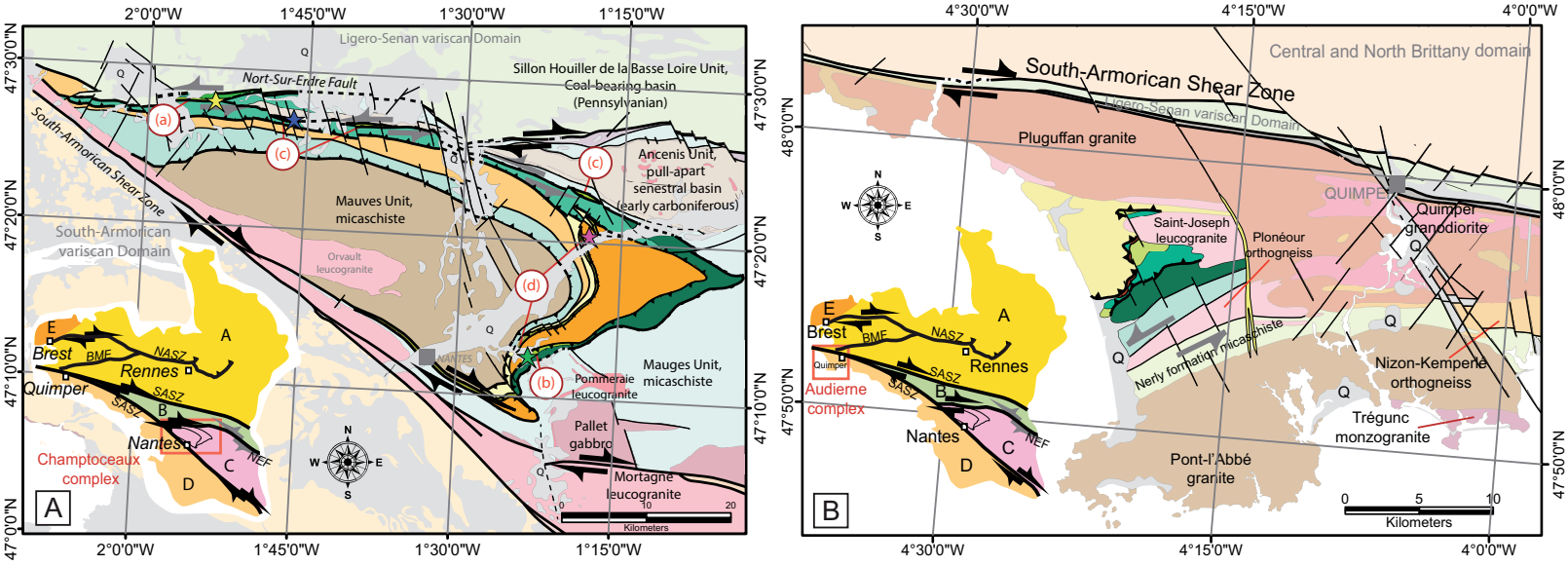

Champtoceaux Complex

- Pont de Barel Formation, amphibolites
- Drain Formation, metagabbro and amphibolite (upper Devonian)
- Le Hâvre Formation, micaschiste et amphibolite
- Champtoceaux Formation, orthogneiss
- Folies Siffait Formation, amphibolite
- Saint-Mars-du-Désert Formation
  - micaschiste
  - orthogneiss
- Cellier Formation micaschiste et leptynite
- Peridotite and serpentinite

Sampling areas

- (a) Pont de Barel
- (b) Butte de la Roche
- (c) L'orgerais
- (d) Folies Siffait

Audierne Complex

Ophiolitic unit

- Penhors formation, micaschiste
- Languidou-Penhors orthogneiss
- Ty-Lan serpentinites and peridotite
- Peumerit formation, amphibolite and metagabbro
- Tréogat formation, amphibolite, prasinite and ovardite
- Trunvel formation, micaschiste

Dextral sens of shear of the SASZ (Mississipian to Pennsylvanian)

Senestral sens of shear

Armorican Massif Domains

- A Central and North Brittany domain (Armorica microplate)
- B Ligéro-sénan variscan domain
- C Nantais domain
- D South armorican variscan domain
- E Léon variscan domain

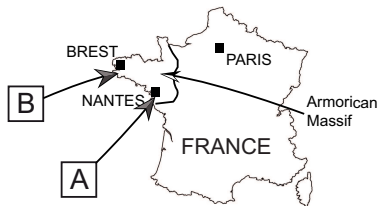

Fig. 1

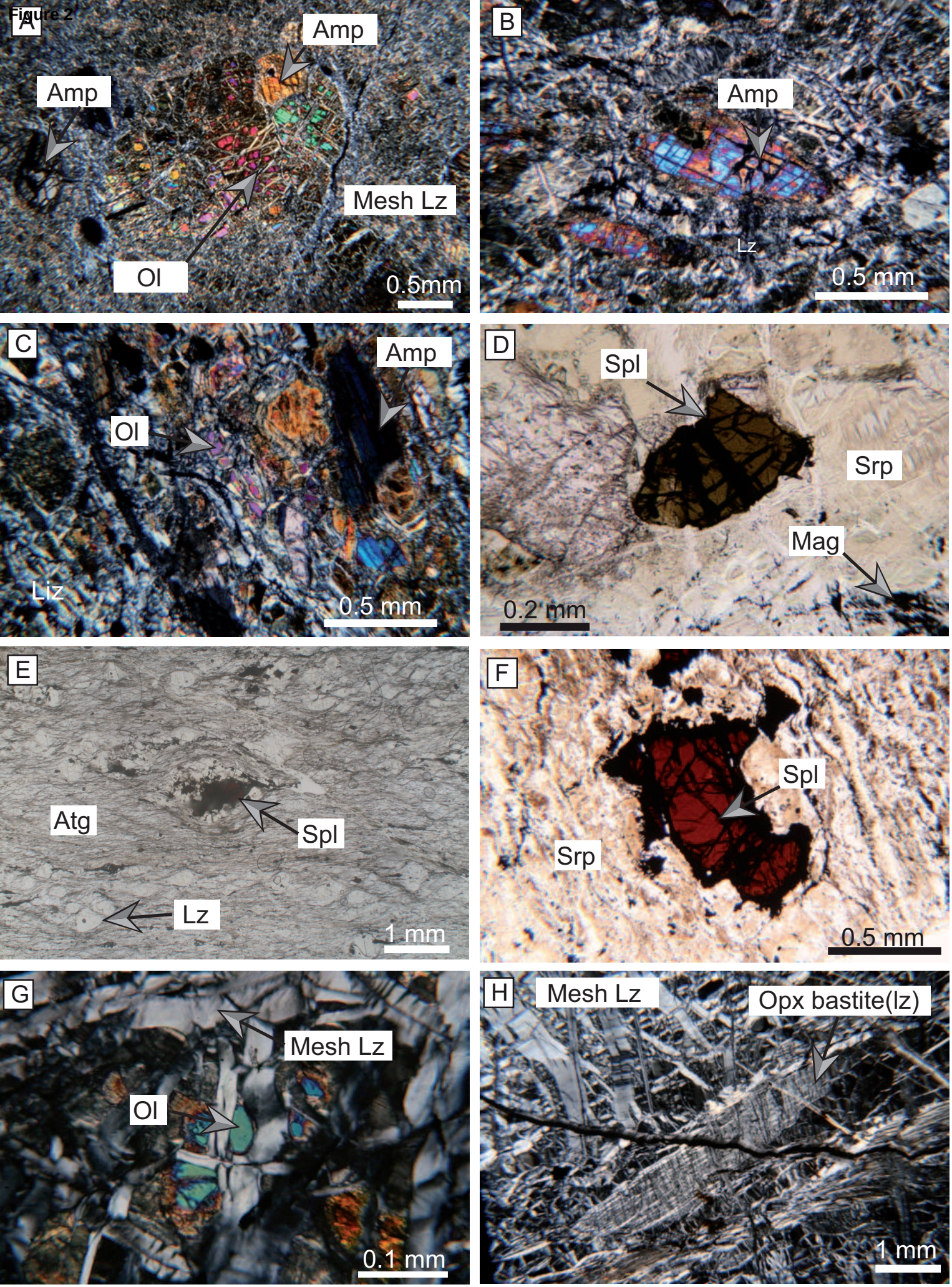
Figure 2
A
Amp
Amp
Mesh Lz
Ol
0.5mm
B
Amp
Lz
0.5 mm
C
Amp
Ol
Liz
0.5 mm
D
Spl
Srp
Mag
0.2 mm
E
Atg
Spl
Lz
1 mm
F
Spl
Srp
0.5 mm
G
Mesh Lz
Ol
0.1 mm
H
Mesh Lz
Opx bastite(lz)
1 mm

Fig. 2

Figure 3

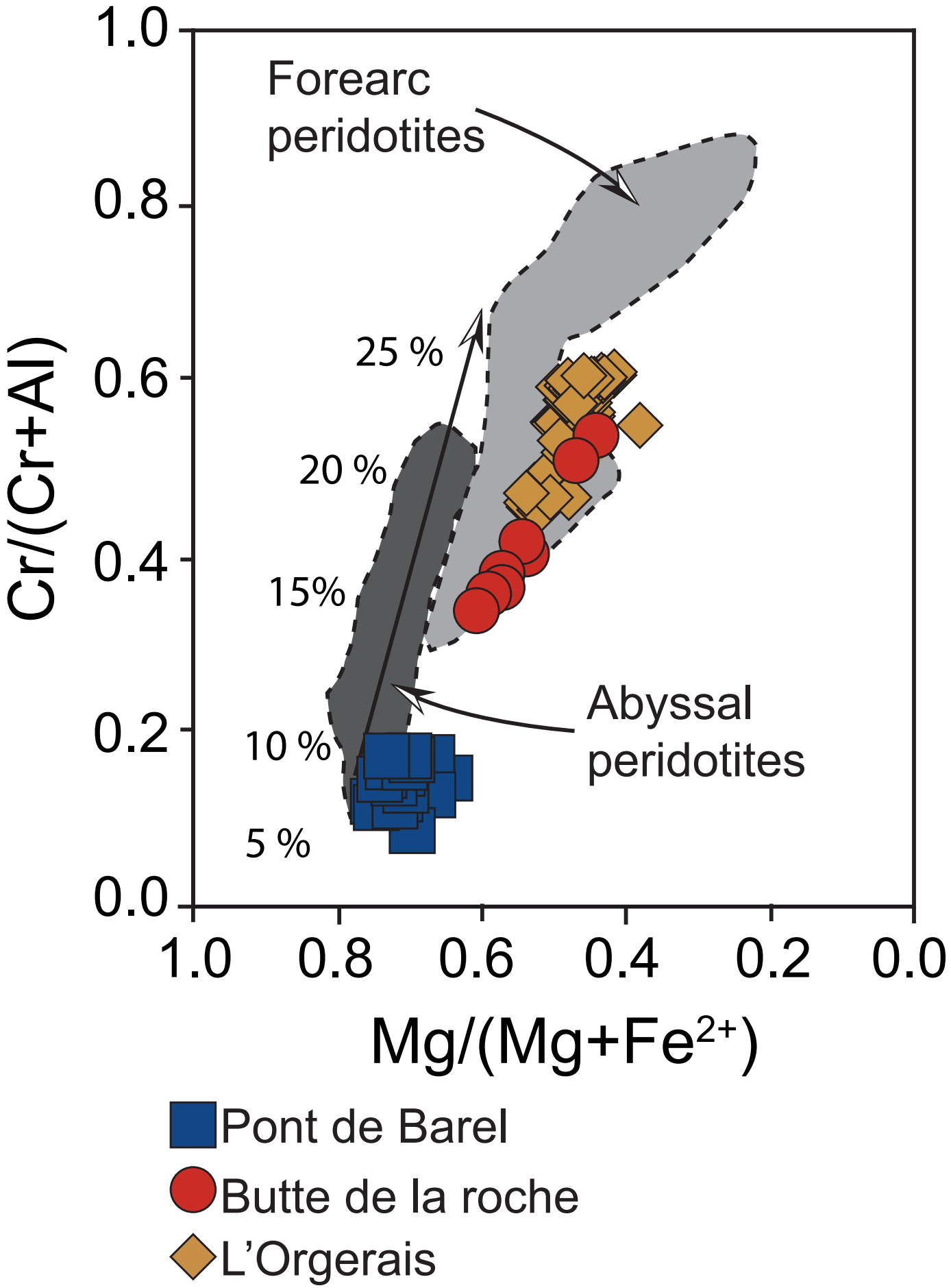

Fig. 3

Figure 4

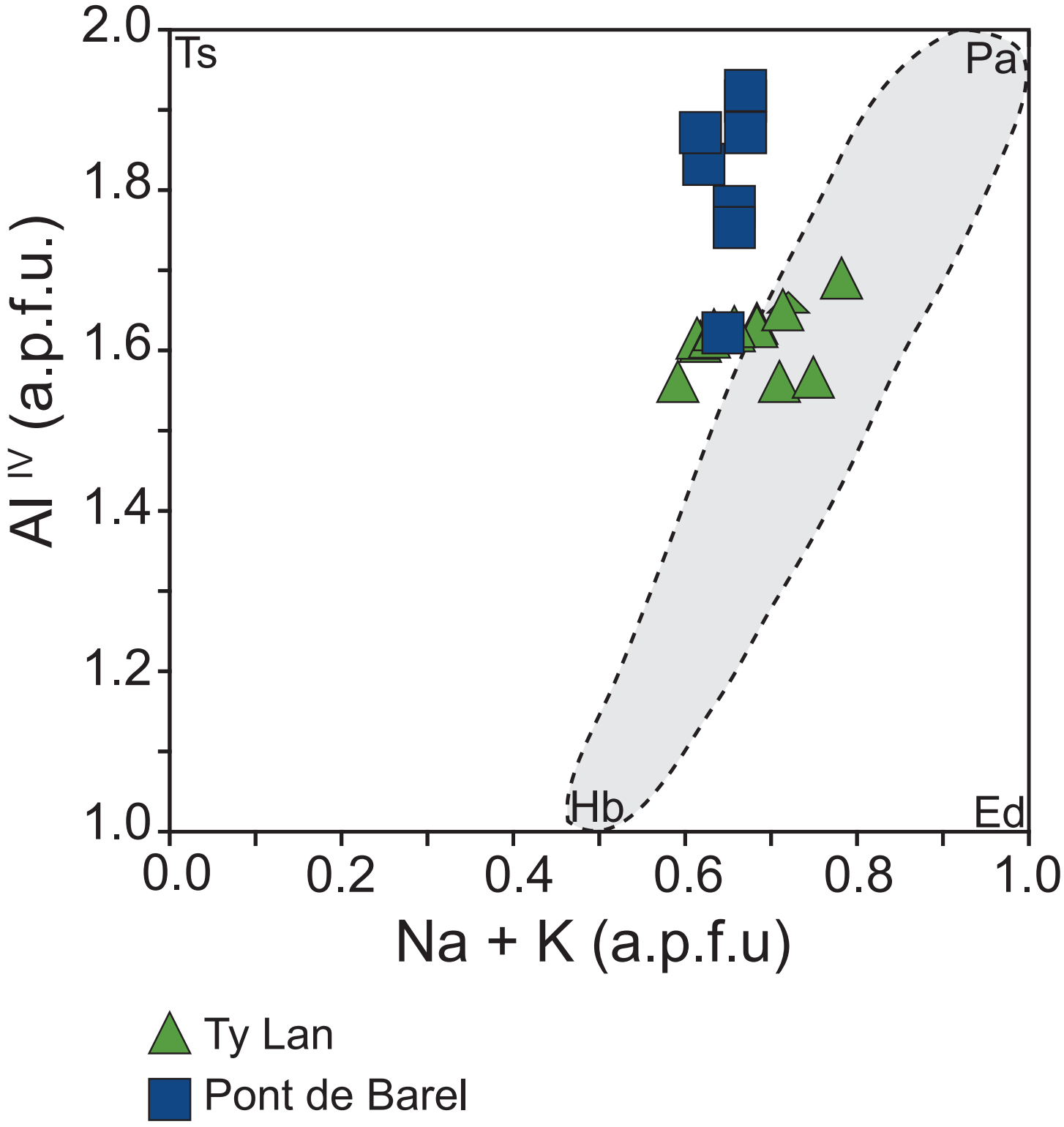

Fig. 4

Figure 5

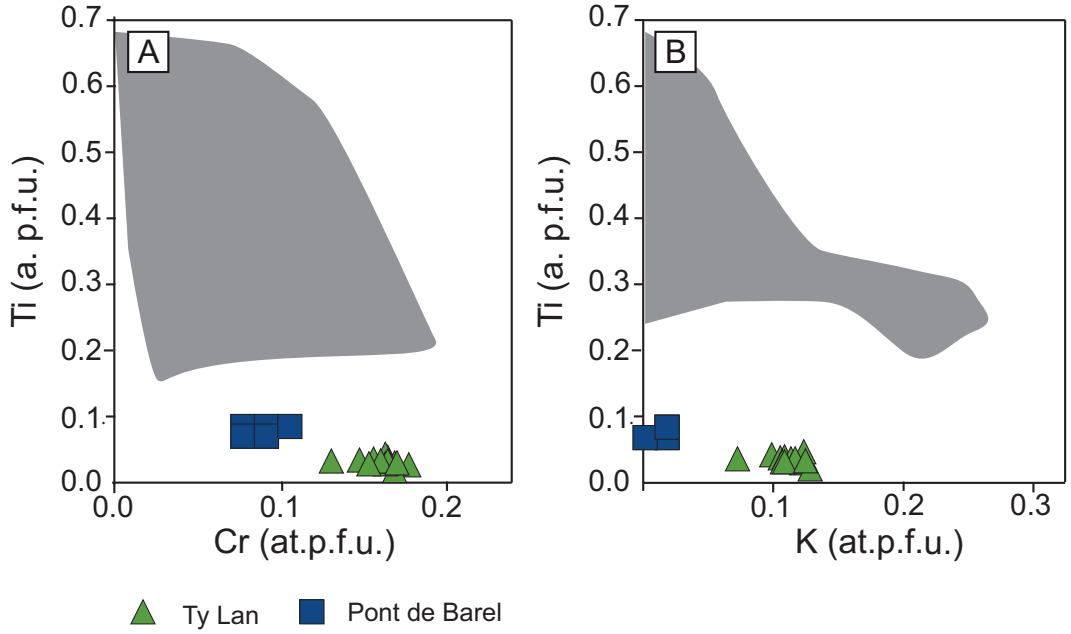

Fig. 5

Fig. 5

Figure 6

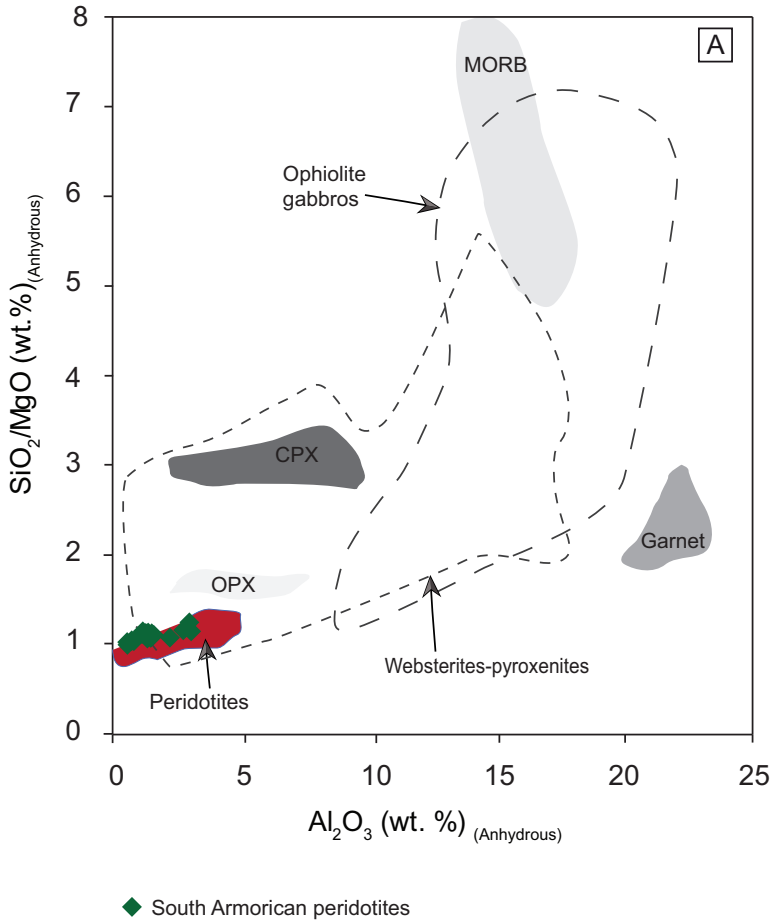

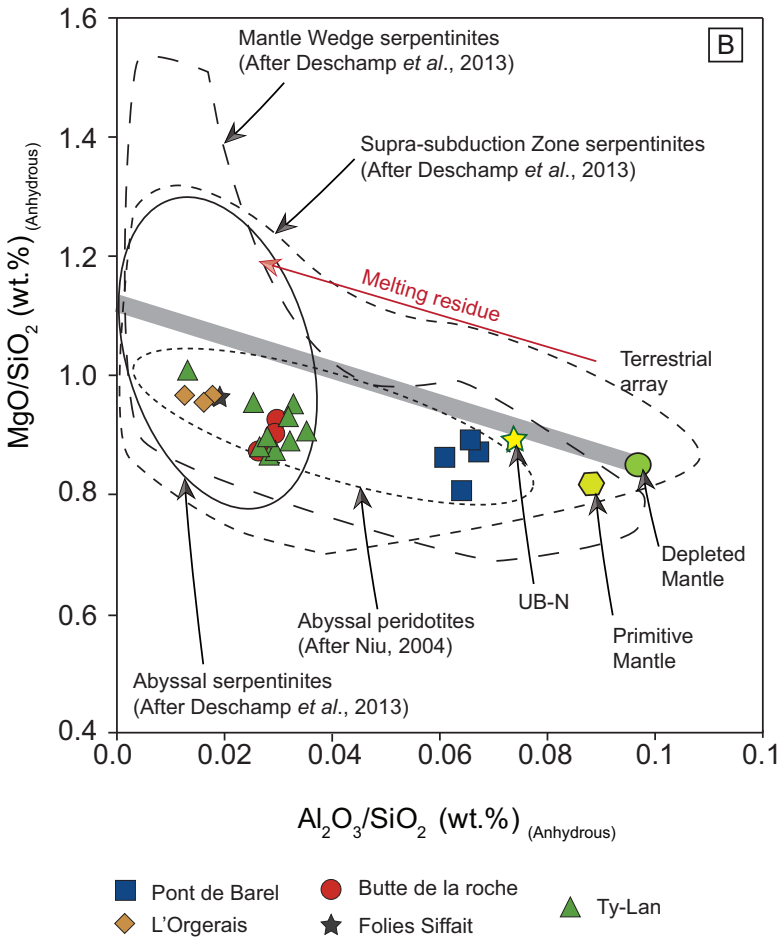

South Armorican peridotites

Pont de Barel
L'Orgerais
Butte de la roche
Folies Siffait
Ty-Lan

Fig. 6

Figure 7

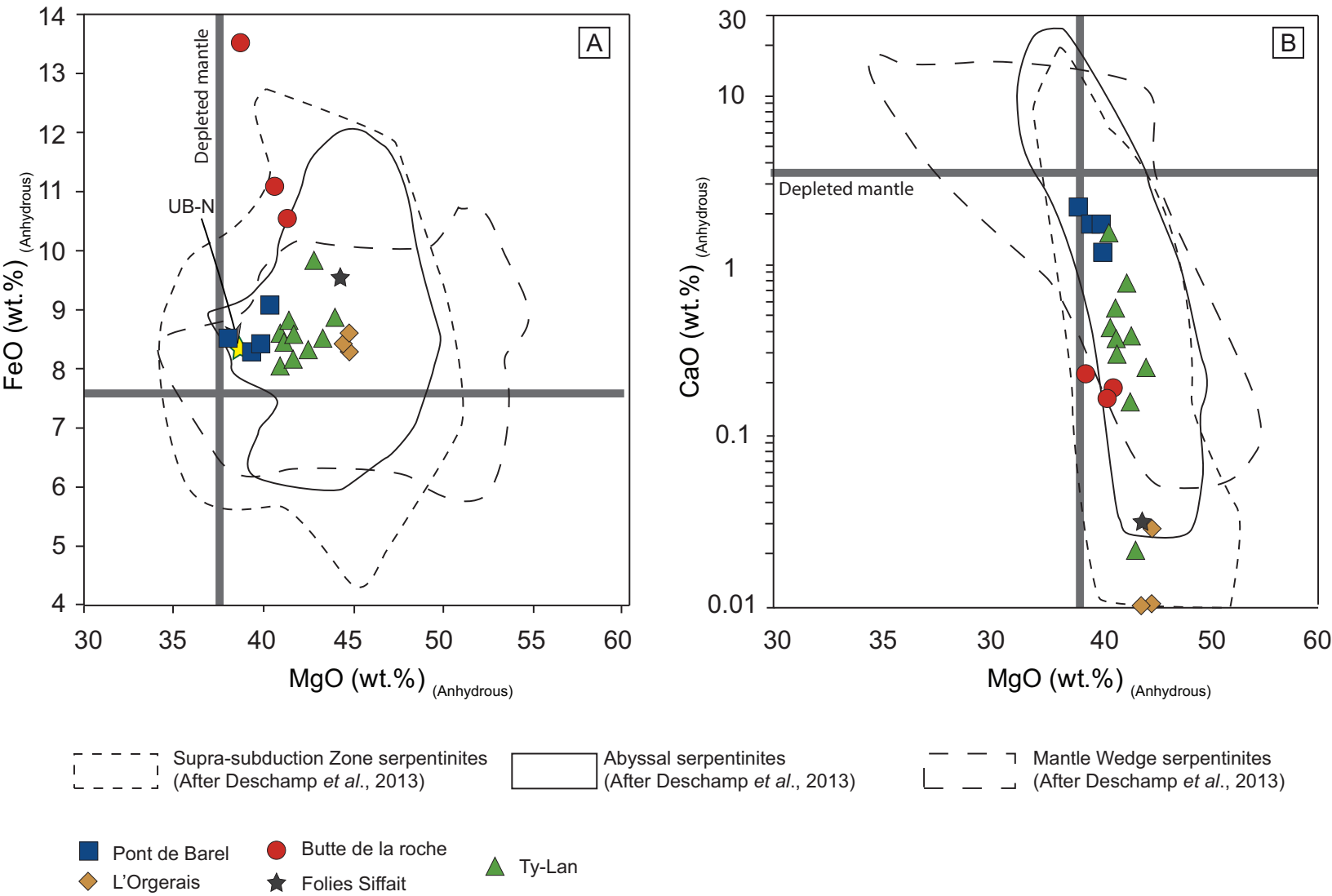

Fig. 7

Figure 8

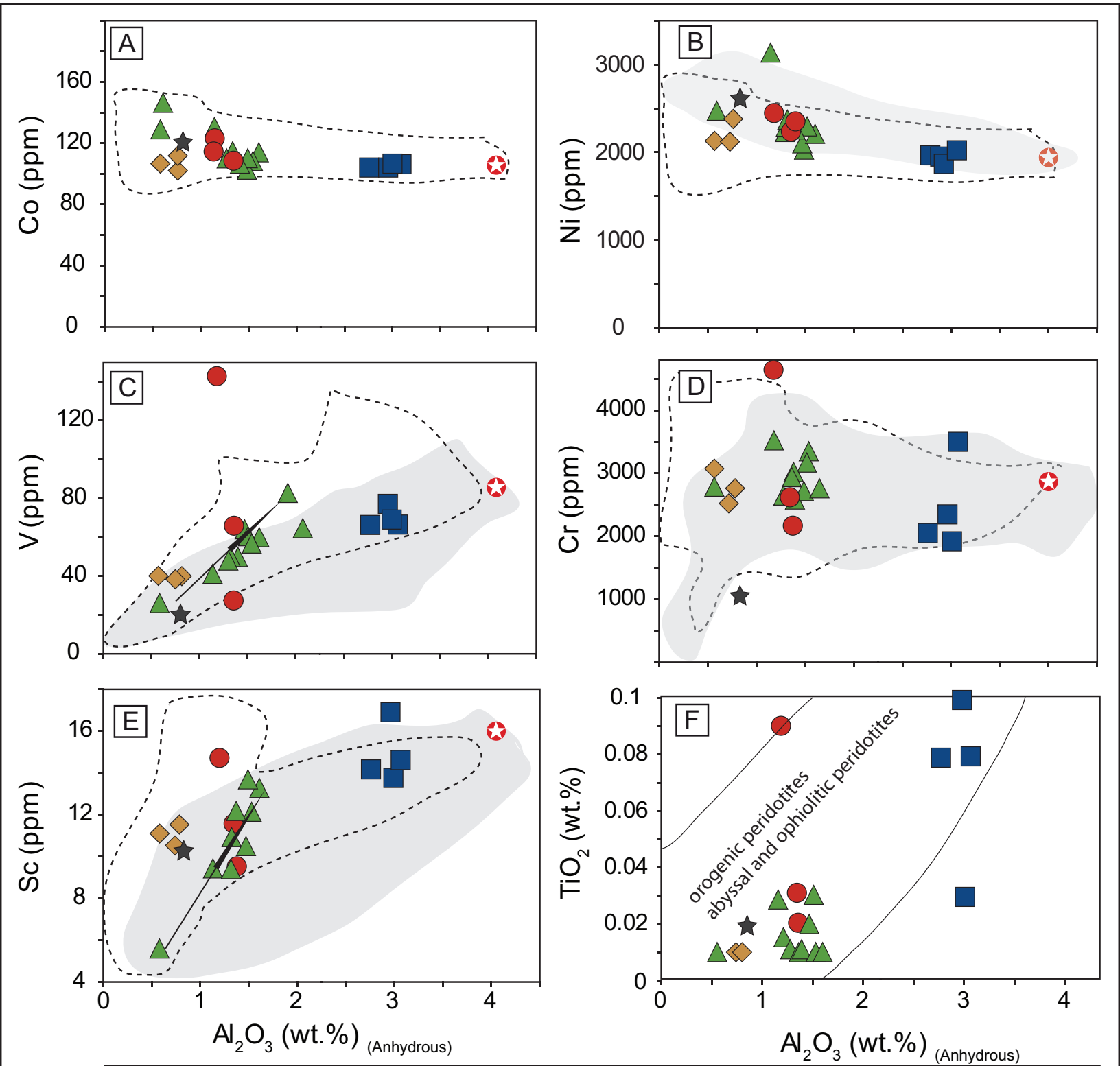

Fig. 8

Figure 9

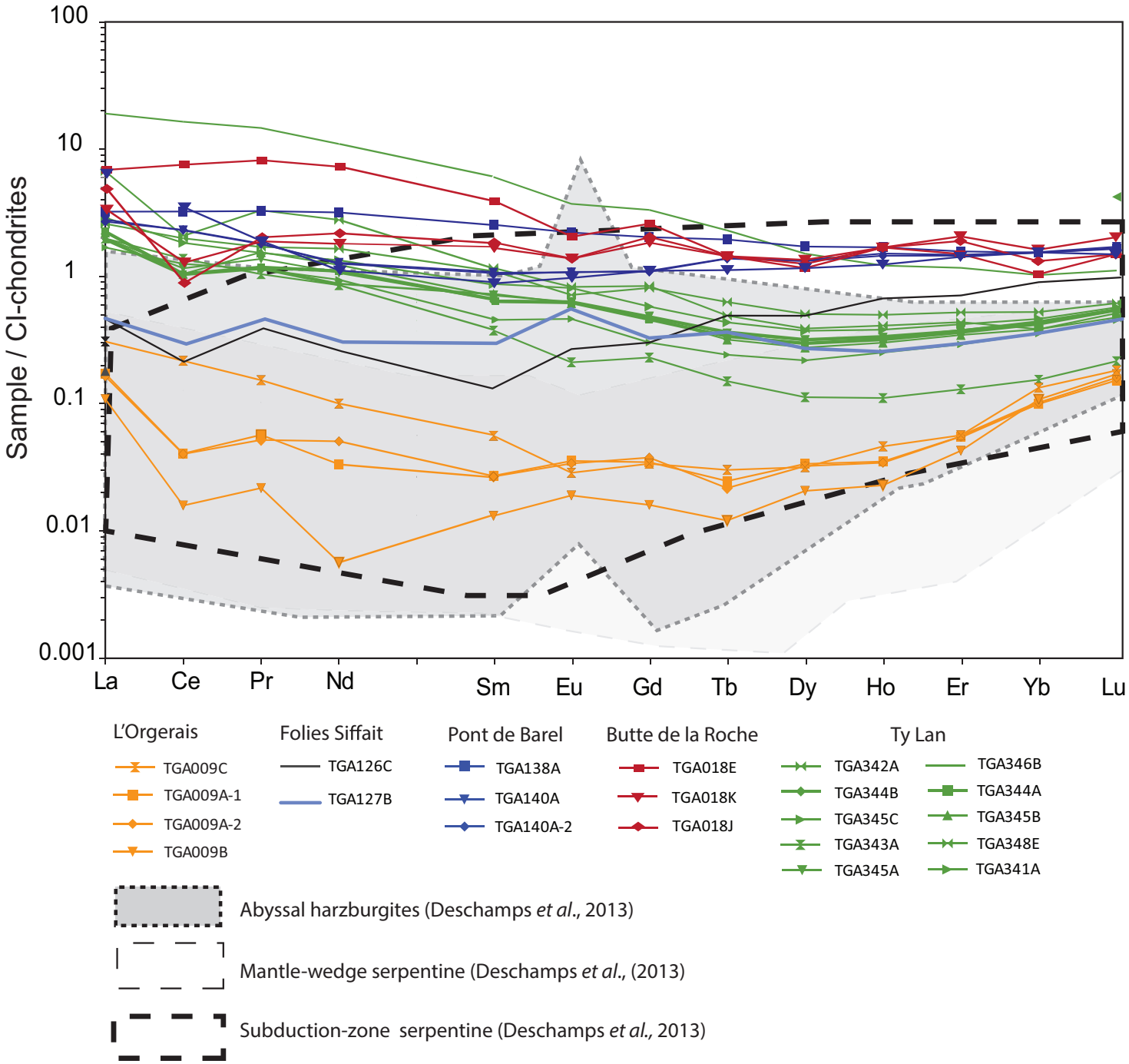

Fig. 9

Figure 10

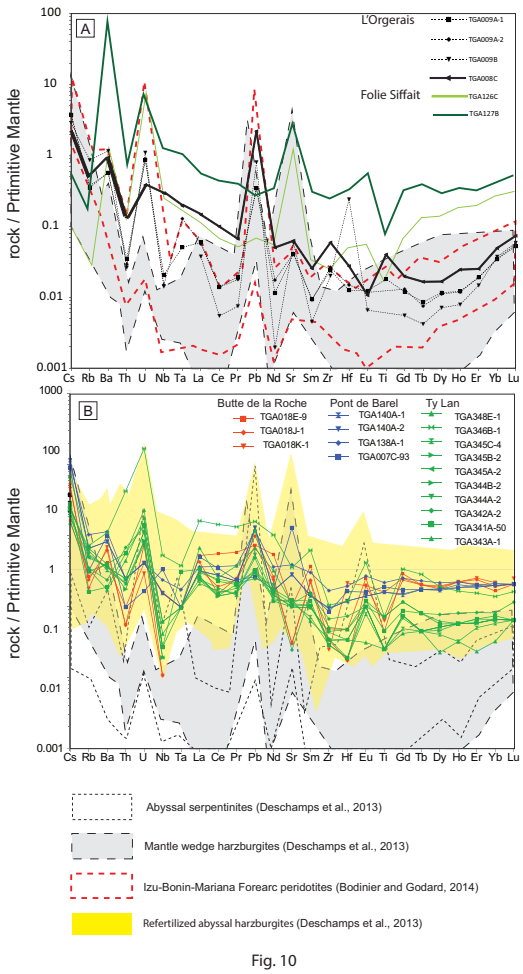

Fig. 10

Figure 11

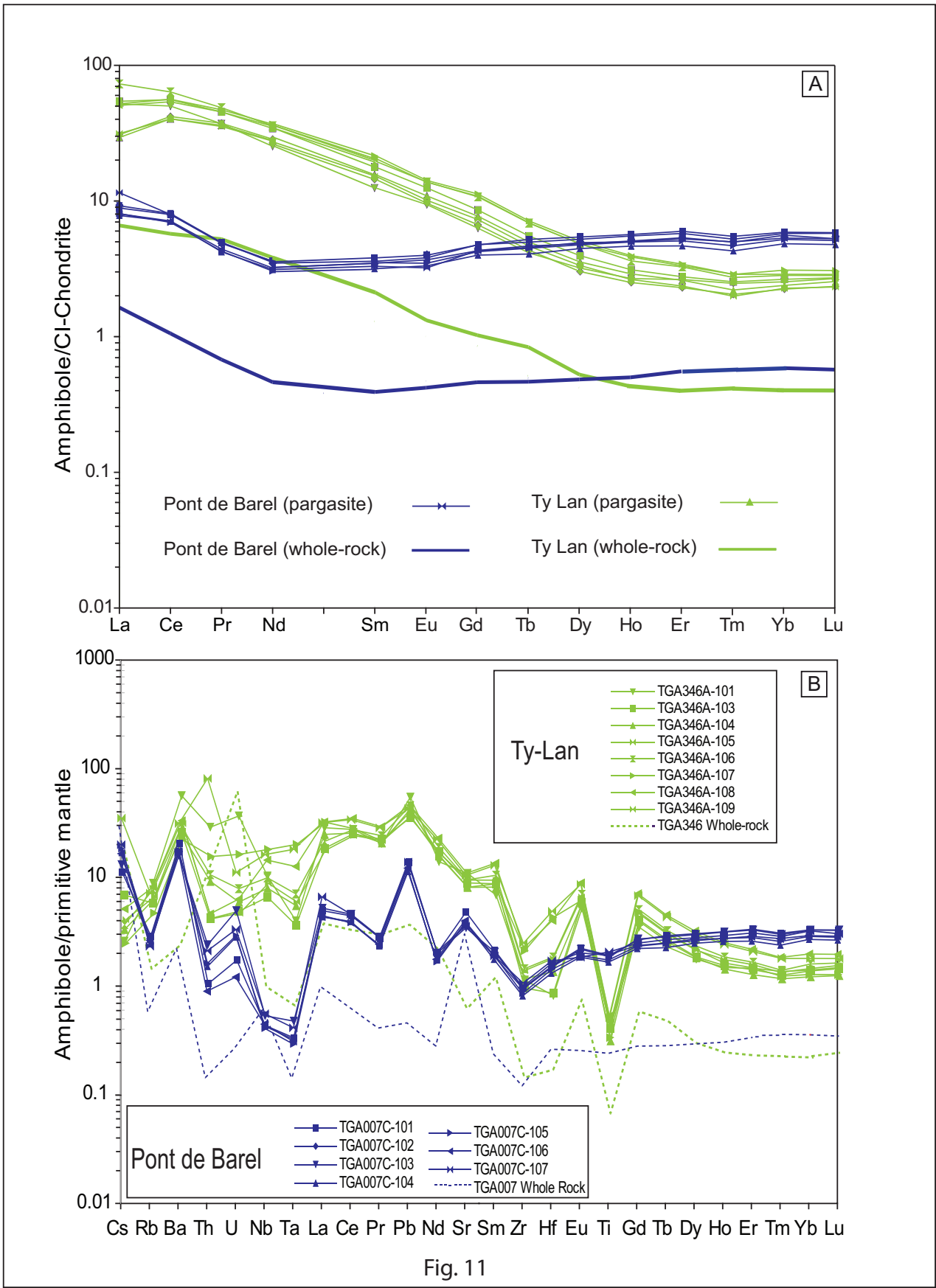

Fig. 11

Figure 12

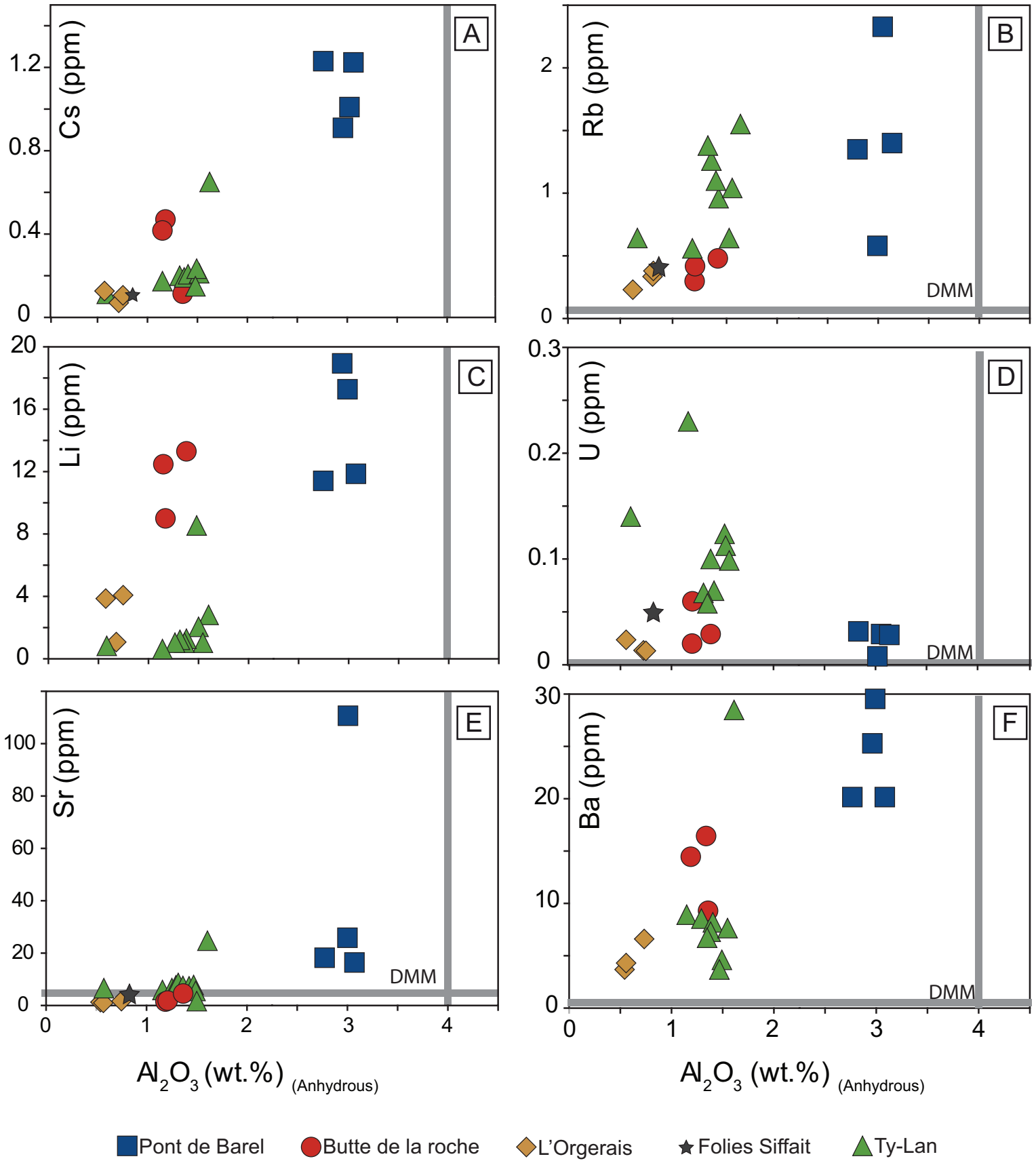

Fig. 12

Figure 13

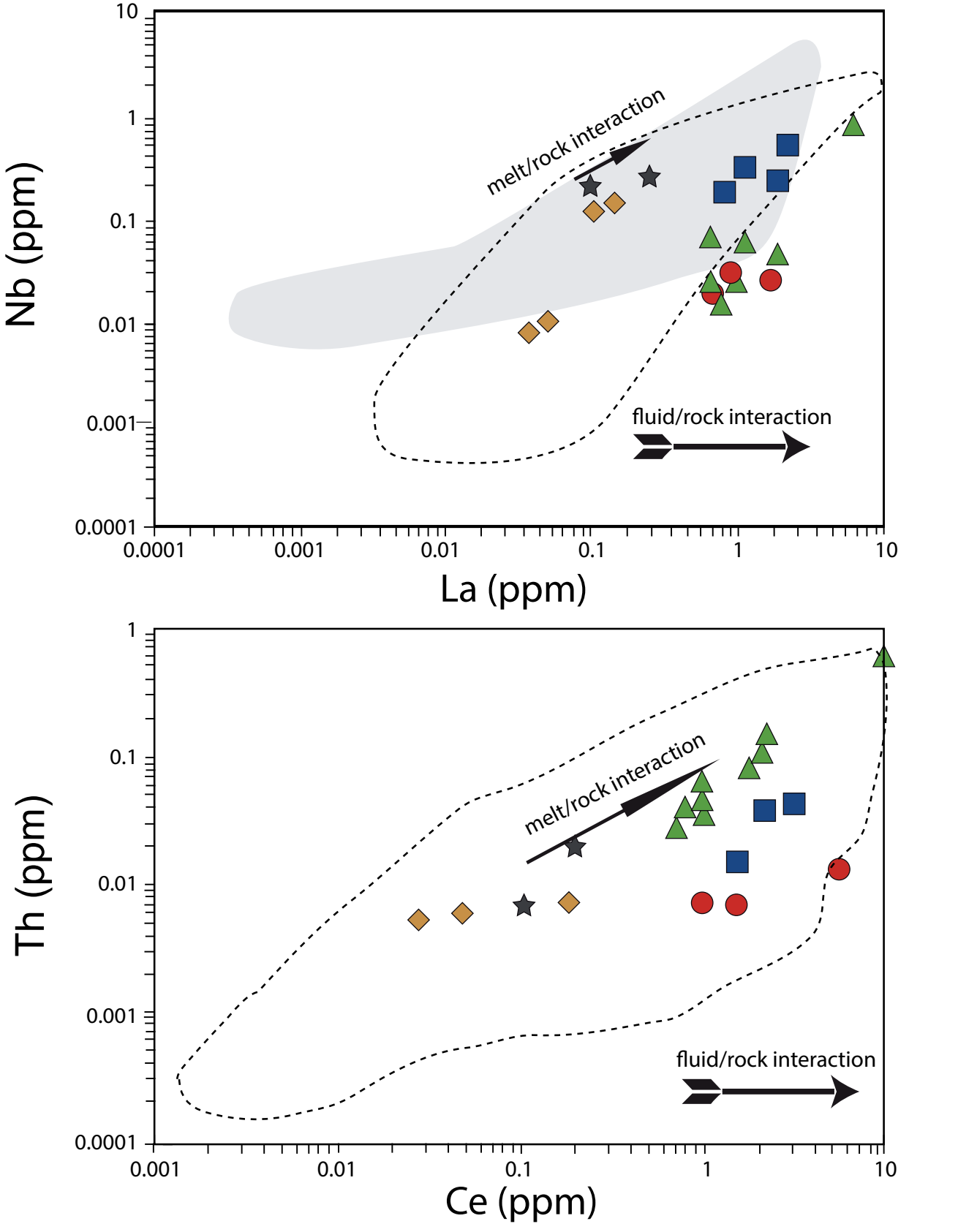

Fig. 13

Figure 14

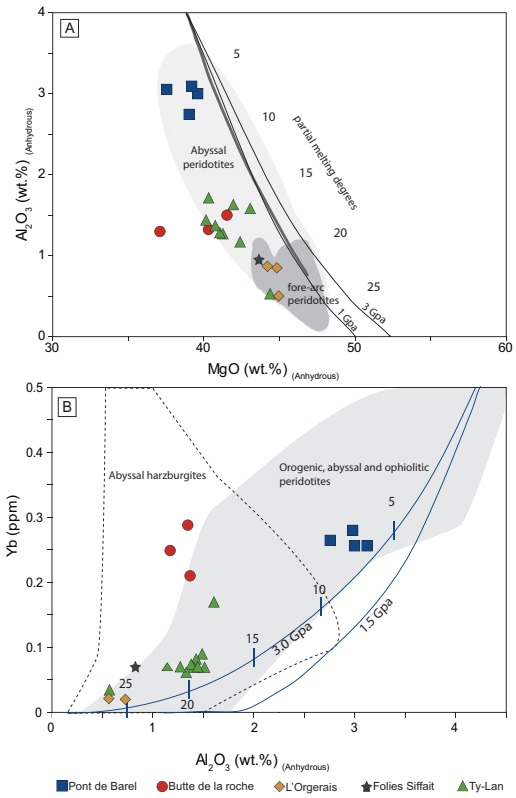

Fig. 14

Table 1

Click here to download Table: Table 1.docx

Table 1

Representative electron microbrobe analyses of olivine.

Locality	Ty-Lan															Folies Siffait					
Sample name	TGA 346 A															TGA 126 C					
Analysis number	17	18	19	2	20	3	31	32	33	34	35	4	46	5	7	5	6	22	21	3	4
Major elements (wt.%)																					
SiO_2	40.66	40.9	40.89	40.93	40.8	40.77	41.31	41.29	41.04	40.48	40.77	41.4	40.78	41.29	41.16	41.27	41.34	40.94	41.42	41.5	40.67
TiO_2		0.01		0.04		0.01	0.03			0.07	0.07	0.04	0.05		0.01	0.02	0.03	0	0	0.03	0.03
MnO	0.17	0.11	0.18	0.14	0.18	0.2	0.16	0.17	0.17	0.19	0.17	0.19	0.2	0.22	0.15	0.23	0.17	0.19	0.17	0.19	0.18
FeO	10.34	9.54	10.75	9.18	9.64	9.68	9.49	10.07	9.46	10.12	9.68	9.36	10.65	10.07	9.52	10.62	10.61	10.69	10.78	10.73	10.89
NiO	0.38	0.4	0.39	0.34	0.35	0.37	0.38	0.37	0.37	0.37	0.42	0.36	0.32	0.31	0.37	0.31	0.33	0.32	0.43	0.27	0.39
MgO	48.87	49.58	48.59	49.93	49.5	49.55	50.13	49.54	49.51	49.47	49.65	49.49	48.16	48.79	49.41	48.13	48.38	48.46	48.7	48.77	48.85
Total	100.41	100.6	100.88	100.57	100.53	100.6	101.58	101.45	100.59	100.79	100.82	100.85	100.21	100.73	100.64	100.63	100.91	100.63	101.52	101.54	101.06
Mg no	89	90	89	91	90	90	90	90	90	90	90	90	89	90	90	89	89	89	89	89	89

Mg no = 100*MgO/(Mgo+FeO)

Table 2

Click here to download Table: Table 2.docx

Table 2

Representative electron microbrobe analyses of Cr-spinel.

Locality	Pont de Barel							Butte de la Roche									L'Orgerais													
Sample name	TGA007C							TGA387A									TGA008B				TGA009C					TGA023A				
Analysis number	65	58	48	36	42	43	44	13	4	14	3	5	16	1	17	2	1	2	3	4	6	7	8	9	10	11	12	13	14	15
SiO_2	0.13	0.13	0	0.03	0.06	2.14				0	0.04	0	0.03	0.03	0		0.04	0	0	0.04	0.08	0	0	0	0	0.09	0	0	0.05	0.05
TiO_2	0.05	0.01	0	0.06	0.05	0.01	0.01	0.09	0.1	0.09	0.15	0.13	0.09	0.13	0.11	0.11	0.1	0.04	0.08	0.07	0.05	0.01	0	0.07	0.04	0.09	0.04	0.03	0.06	0.07
Al_2O_3	54.65	53.23	54.95	52.85	53.58	55.3	48.18	35.52	31.72	27.06	32.56	24.68	37.4	23.34	35.91	23.1	25.56	21.41	25.47	19.77	27.4	29.64	30.63	28.43	26.12	21.12	21.93	21.7	20.95	20.94
Cr_2O_3	12.37	12.34	7.95	12.18	12.04	10.32	12.57	29.97	33.28	37.05	32.85	39.21	27.82	40.69	29.31	41.17	42.69	46.32	43.07	40.52	39.47	37.02	37	38.38	40.9	45.94	46.39	46.18	45.83	46.24
MnO	0.14	0.12	0.08	0.14	0.1	0.14	0.43	0.19	0.26	0.34	0.26	0.31	0.2	0.26	0.16	0.27	0.19	0.29	0.16	0.34	0.25	0.22	0.24	0.28	0.29	0.21	0.24	0.3	0.3	0.29
FeO	16.82	15.44	14.56	15.74	15.67	14.77	19.1	20.43	21.98	23.34	21.76	24.39	19.44	24.27	20.01	24.98	20.67	22.63	20.82	28.78	21.91	21.11	21.16	21.21	22.23	22.98	21.74	22.25	22.54	22.8
Fe_2O_3	1.24	2.53	0.04	3.19	3.51	2.82	4.21	3.22	3.96	4.38	3.48	4.24	3.42	3.59	3.44	4.56	1.55	2.1	1.28	8.32	2.93	3.16	2.37	2.92	2.71	1.99	1.79	2.11	2.12	1.77
NiO	0.32	0.33	0.39	0.37	0.34	0.34	0.33	0.2	0.12	0.15	0.16	0.06	0.14	0.01	0.15	0.1	0.02	0.06	0.02	0.02	0.07	0.01	0.12	0.04	0.09					
MgO	16.35	17.36	18.06	17.49	17.98	18.21	17.26	12.93	11.95	10.75	12.01	9.75	13.8	9.21	13.37	9.4	11.04	9.42	10.69	8.61	11.09	11.93	11.59	11.62	10.53	9.1	10.03	9.79	9.28	9.02
Total	100.96	99.28	97.98	99.16	100.17	99.46	100.44	99.4	99.5	98.87	99.83	98.63	98.99	98.04	99.12	99.25	100.46	100.42	100.46	99.02	100.65	100.27	101	100.31	100.49	99.79	100.55	100.46	99.29	99.65
Mg#	0.65	0.7	0.69	0.71	0.72	0.73	0.67	0.57	0.54	0.51	0.54	0.47	0.61	0.45	0.59	0.45	0.51	0.45	0.49	0.43	0.51	0.54	0.52	0.53	0.49	0.44	0.47	0.46	0.45	0.43
Cr#	0.13	0.13	0.09	0.13	0.13	0.11	0.15	0.36	0.41	0.48	0.4	0.52	0.33	0.54	0.35	0.54	0.53	0.59	0.53	0.58	0.49	0.46	0.45	0.48	0.51	0.59	0.59	0.59	0.59	0.6

Mg# = Mg/(Mg+Fe2+); Cr# = Cr/(Cr+Al); Trivalent iron content calculated by assuming stoichiometry

Table 3

Click here to download Table: Table 3.docx

Table 3

Representative electron microprobe analyses of paragasite (wt%)

Locality	Pont de Barel							Butte de la Roche							
Sample name	TGA007C							TGA346A							
Analysis number	32	85	86	87	88	89	91	9	45	42	41	38	21	11	37
SiO_2	42.96	44.35	44.14	43.71	44.32	45.03	43.83	44.79	45.22	44.54	44.77	44.59	44.64	45.06	44.81
TiO_2	0.65	0.69	0.63	0.78	0.72	0.69	0.71	0.26	0.19	0.2	0.13	0.29	0.22	0.22	0.2
Al_2O_3	13.83	14.25	14.38	14.56	14.19	12.87	14.27	12.75	12.00	12.58	12.7	12.3	12.6	12.6	12.13
Cr_2O_3	0.83	0.75	0.74	0.79	0.82	0.78	0.93	1.49	1.57	1.51	1.51	1.47	1.46	1.28	1.522
MnO	0.09	0.09	0.08	0.06	0.01	0.02	0.08	0.08	0.08	0.04	0.07	0.04	0.03	0.09	0.1
FeO*	0.37	1.67	0.79	0.77	2.06	2	0.76	1.40	1.42	1.3	0.82	1.18	0.73	0.77	0.48
Fe_2O_3*	4.65	2.8	3.92	4.12	2.36	2.34	4.16	2.83	2.57	2.77	3.24	3.08	3.14	3.6	3.9
NiO	0.19	0.09	0.13	0.14	0.05	0.05	0.08	0.12	0.03	0.15	0.11	0.05	0.11	0.17	0.08
MgO	17.97	18.01	18.05	18.11	17.89	18.39	17.97	18.46	18.82	18.34	18.59	18.64	18.5	18.56	19.1
CaO	12.62	12.57	12.63	12.57	12.53	12.77	12.59	12.56	12.69	12.55	12.1	12.69	12.57	12.46	12.12
Na_2O	2.59	2.65	2.62	2.73	2.66	2.59	2.58	2.46	2.41	2.31	2.23	2.39	2.31	2.35	2.21
K_2O	0.1	0.11	0.08	0.1	0.1	0.08	0.11	0.52	0.6	0.61	0.61	0.6	0.57	0.43	0.6
H_2O^+	2.12	2.13	2.13	2.12	2.13	2.13	2.13	2.12	2.12	2.12	2.13	2.12	2.13	2.13	2.13
Total	98.97	100.18	100.3	100.59	99.83	99.76	100.23	99.87	99.78	99.07	99.04	99.56	99.05	99.83	99.41
Structural formulae															
Si(T)	6.14	6.24	6.2	6.13	6.26	6.36	6.17	6.33	6.404	6.353	6.367	6.336	6.354	6.362	6.356
Al(T)	1.86	1.76	1.8	1.87	1.74	1.64	1.83	1.66	1.594	1.646	1.632	1.662	1.646	1.635	1.643
T (sum)	8	8	8	8	8	8	8	8	8	8	8	8	8	7.999	8
(C)Ti	0.07	0.07	0.07	0.08	0.08	0.07	0.08	0.028	0.02	0.022	0.014	0.031	0.024	0.024	0.022
(C)Al	0.47	0.6	0.58	0.54	0.62	0.5	0.54	0.466	0.409	0.47	0.497	0.407	0.469	0.469	0.386
(C)Cr	0.09	0.08	0.08	0.09	0.09	0.09	0.1	0.167	0.176	0.17	0.17	0.166	0.164	0.143	0.171
(C)Fe^{3+}	0.5	0.3	0.41	0.44	0.25	0.25	0.44	0.302	0.274	0.298	0.347	0.329	0.337	0.382	0.416
(C)Ni	0.02	0.01	0.01	0.02	0.01	0.01	0.01	0.014	0.004	0.018	0.011	0.005	0.013	0.02	0.009
(C)Fe^{2+}	0.02	0.16	0.07	0.05	0.2	0.21	0.06	0.13	0.143	0.123	0.02	0.114	0.067	0.054	
(C)Mg	3.83	3.78	3.78	3.79	3.76	3.87	3.77	3.893	3.973	3.899	3.942	3.948	3.926	3.908	3.997
C (sum)	5	5	5	5	5	5	5	5	4.999	5	5.001	5	5	5	5.001
(B)Mn^{2+}	0.01	0.01	0.01	0.01	0	0	0.01	0.009	0.01	0.005	0.009	0.006	0.004	0.011	0.013
(B)Fe^{2+}	0.02	0.04	0.03	0.04	0.05	0.03	0.03	0.035	0.025	0.033	0.079	0.026	0.02	0.038	0.057
(B)Ca	1.93	1.9	1.9	1.89	1.9	1.93	1.9	1.905	1.925	1.918	1.844	1.932	1.917	1.885	1.842
(B)Na	0.04	0.06	0.07	0.06	0.06	0.04	0.06	0.051	0.04	0.044	0.069	0.037	0.058	0.066	0.045
B (sum)	2	2	2	2	2	2	2	2	2	2	2.001	2.001	1.999	2	2
(A)Na	0.68	0.67	0.65	0.68	0.67	0.67	0.64	0.626	0.623	0.596	0.547	0.624	0.581	0.579	0.563
(A)K	0.02	0.02	0.01	0.02	0.02	0.01	0.02	0.094	0.108	0.11	0.112	0.109	0.105	0.078	0.109
A (sum)	0.7	0.69	0.66	0.7	0.69	0.69	0.66	0.72	0.731	0.706	0.659	0.733	0.686	0.657	0.672
(A)Na + (B)Na	0.718	0.723	0.713	0.743	0.728	0.708	0.704	0.677	0.663	0.64	0.616	0.661	0.639	0.645	0.608

Structural formulae were calculated on 22 oxygen atoms, with the Excel spreadsheet of Locock (2014)

Table 4

Click here to download Table: Table 4.docx

Table 4

Bulk-rock analyses of south-Armorican peridotites and international rock standards

Locality	Pont de Barel				Butte de la Roche			L'Orgerais				Ty-Lan									
Sample name	TGA140A	TGA140Ad	TGA138A	TGA007A	TGA018E	TGA018J	TGA018K	TGA009C	TGA009B	TGA008C	TGA009A	TGA348E	TGA346B	TGA345C	TGA345B	TGA345A	TGA344B	TGA344A	TGA342A	TGA341A	TGA343A
wt.%																					
SiO_2	40.11	40.17	41.51	39.57	38.90	37.52	38.21	40.64	N.A.	40.41	40.70	38.72	39.89	39.56	39.83	40.74	39.88	39.77	40.13	39.47	38.02
TiO_2	0.080	0.081	0.109	0.098	0.025	0.091	0.030	0.009	N.A.	0.009	0.004	0.026	0.026	0.010	0.010	0.014	0.014	0.013	0.032	0.015	0.012
Al_2O_3	2.44	2.72	2.68	2.65	1.18	1.05	1.15	0.65	N.A.	0.68	0.51	0.99	1.42	1.13	1.11	1.21	1.32	1.21	1.35	1.28	0.51
FeO	7.24	7.40	7.47	7.98	9.21	11.52	9.44	7.33	N.A.	7.39	7.27	8.43	7.56	7.42	7.25	6.92	7.05	7.16	7.52	7.20	8.18
MnO	0.09	0.09	0.10	0.09	0.08	0.10	0.08	0.07	N.A.	0.08	0.07	0.10	0.11	0.10	0.10	0.10	0.08	0.09	0.08	0.09	0.08
MgO	34.6	35.2	33.8	35.4	36.1	32.9	34.6	38.8	N.A.	39.1	39.6	36.7	35.9	35.2	35.3	35.2	35.3	35.1	38.0	36.7	37.7
CaO	1.54	1.56	1.98	1.05	0.17	0.20	0.15	0.01	N.A.	0.01	0.03	0.14	1.36	0.47	0.29	0.36	0.26	0.30	0.02	0.66	0.21
Na_2O	<0.003	<0.003	0.207	0.092	<0.003	0.009	0.009	<0.003	N.A.	<0.003	0.003	0.015	0.099	0.071	0.063	0.059	0.021	0.026	0.005	0.010	0.007
K_2O	0.032	0.032	0.103	<0.014	<0.014	0.026	0.025	<0.014	N.A.	<0.014	<0.014	<0.014	0.037	0.036	0.033	0.022	0.024	0.020	N.A.	<0.014	<0.014
P_2O_5	<0.013	<0.013	0.017	0.025	<0.013	0.020	0.019	<0.013	N.A.	<0.013	<0.013	0.036	0.044	0.014	0.020	0.020	<0.013	0.014	0.019	0.018	0.045
LOI	11.57	11.57	11.57	12.14	12.43	15.32	15.28	12.43	N.A.	12.41	10.97	13.84	12.75	15.13	15.16	14.58	15.27	15.52	11.96	13.71	14.30
ppm																					
Li	11.48	11.86	17.28	18.97	13.35	9.03	11.78	3.99	5.47	0.83	3.86	0.52	2.82	0.92	0.99	1.03	1.11	1.15	2.05	8.58	0.85
Be	<0.24	<0.24	<0.24	<0.24	0.47	0.61	<0.24	<0.24	<0.24	<0.24	<0.24	<0.24	1.40	<0.24	<0.24	<0.24	<0.24	<0.24	<0.24	<0.24	<0.24
Sc	12.6	13.0	12.2	14.9	10.0	12.5	8.0	9.7	9.3	9.3	10.0	8.2	11.5	9.4	9.0	10.3	10.4	10.4	12.1	12.1	4.8
V	66.6	66.5	68.4	76.9	27.4	142.9	66.0	39.2	34.8	38.1	39.3	40.6	59.0	50.1	48.3	51.8	56.3	50.0	59.0	62.6	24.4
Cr	2050	2074	1918	2360	2183	4647	2597	2780	2353	2536	3045	3519	2730	2882	2622	3038	3321	2599	3260	2704	2800
Co	99	100	97	97	100	108	114	106	107	96	101	123	106	108	104	102	101	103	97	103	122
Ni	2004	2042	1947	1997	2250	2452	2366	2374	2390	2096	2153	3103	2200	2313	2225	2221	2289	2274	2001	2045	2449
Zn	53	52	53	46	49	74	55	52	68	51	37	53	37	41	39	40	48	46	41	38	59
Ga	2.55	2.53	2.93	2.85	1.36	1.90	1.39	0.72	0.55	0.67	0.63	1.37	1.73	1.23	1.23	1.37	1.55	1.32	1.59	1.47	0.71
Rb	1.37	1.38	2.34	0.58	0.47	0.41	<0.30	0.35	0.55	0.34	<0.307	0.56	1.53	1.26	1.38	0.96	1.02	1.10	0.65	<0.307	0.62
Sr	18.32	18.23	26.64	16.91	5.38	6.57	5.85	1.39	1.24	1.32	0.87	5.86	23.84	6.13	5.90	5.40	5.23	5.19	0.99	6.73	6.87
Y	2.41	2.42	2.71	2.39	0.04	5.16	4.42	0.21	0.04	0.25	0.06	1.16	2.23	0.41	0.56	0.61	0.60	0.62	0.78	0.61	0.17
Zr	2.51	2.58	4.81	2.04	1.29	0.68	0.47	0.91	<0.30	0.90	<0.30	1.11	2.61	0.56	0.71	0.67	0.95	0.92	1.54	0.57	0.71
Nb	0.24	0.24	0.40	0.05	0.25	0.03	0.02	0.20	<0.01	0.21	<0.01	0.05	1.03	0.03	0.02	0.02	0.03	0.03	0.08	0.03	0.08
Cs	1.23	1.23	1.00	0.91	0.12	0.43	0.47	0.12	0.09	0.07	0.12	0.17	0.65	0.19	0.19	0.14	0.21	0.20	0.14	0.23	0.11
Ba	20.31	20.29	29.75	25.24	8.92	14.57	16.13	6.57	8.07	6.53	3.98	8.58	28.48	6.72	8.48	7.71	7.64	7.53	4.61	3.49	3.15
La	0.64	0.66	0.76	1.12	1.18	0.92	0.70	0.07	<0.03	0.10	0.04	1.59	4.51	0.40	0.52	0.47	0.46	0.53	0.61	0.69	0.47
Ce	1.42	1.41	1.98	1.85	3.24	0.69	0.90	0.08	<0.05	0.12	<0.05	1.27	10.05	0.77	0.64	0.71	0.63	0.64	1.22	1.12	0.84
Pr	0.172	0.171	0.310	0.182	0.524	0.194	0.177	0.029	<0.004	0.032	0.005	0.314	1.393	0.108	0.147	0.130	0.110	0.112	0.162	0.145	0.099
Nd	0.59	0.60	1.49	0.62	2.41	1.01	0.88	<0.09	<0.09	<0.09	<0.09	1.30	5.13	0.44	0.57	0.50	0.40	0.51	0.77	0.63	0.40
Sm	0.14	0.15	0.39	0.16	0.49	0.29	0.27	<0.01	<0.01	<0.01	<0.01	0.18	0.91	0.07	0.11	0.11	0.10	0.09	0.16	0.13	0.06
Eu	0.063	0.062	0.128	0.071	0.118	0.089	0.085	<0.002	<0.002	<0.002	<0.002	0.048	0.216	0.027	0.036	0.037	0.037	0.036	0.041	0.047	0.012
Gd	0.230	0.233	0.417	0.266	0.548	0.421	0.390	<0.008	<0.008	<0.008	<0.008	0.173	0.684	0.062	0.098	0.100	0.099	0.094	0.167	0.119	0.047
Tb	0.052	0.052	0.073	0.054	0.060	0.060	0.061	0.004	<0.002	0.005	<0.002	0.018	0.086	0.009	0.012	0.013	0.014	0.013	0.024	0.016	0.006
Dy	0.34	0.35	0.43	0.35	0.36	0.37	0.39	<0.02	<0.02	<0.02	<0.02	0.10	0.38	0.06	0.07	0.08	0.08	0.08	0.13	0.09	0.03
Ho	0.082	0.086	0.096	0.085	0.002	0.104	0.100	0.003	<0.0022	0.004	<0.0022	0.023	0.069	0.014	0.017	0.019	0.019	0.018	0.028	0.022	0.006
Er	0.241	0.245	0.260	0.262	0.268	0.317	0.339	<0.004	0.007	0.006	0.009	0.072	0.193	0.048	0.057	0.063	0.062	0.060	0.086	0.070	0.021
Yb	0.261	0.266	0.256	0.264	0.210	0.245	0.285	0.021	0.018	0.022	0.018	0.066	0.174	0.065	0.068	0.076	0.076	0.076	0.093	0.082	0.028
Lu	0.042	0.043	0.042	0.044	0.036	0.044	0.052	0.005	0.004	0.005	0.004	0.012	0.028	0.012	0.013	0.014	0.014	0.014	0.016	0.015	0.005
Hf	0.097	0.098	0.162	0.094	0.037	0.442	0.016	0.014	0.074	0.014	<0.01	0.030	0.094	0.010	0.014	0.017	0.025	0.021	0.050	0.012	0.019
Ta	0.010	0.010	0.019	<0.007	0.010	<0.007	<0.007	<0.007	<0.007	0.008	<0.007	<0.007	0.054	0.009	<0.007	<0.007	<0.007	<0.007	0.013	0.036	0.012
W	<0.021	<0.02	<0.02	0.19	0.31	0.22	0.26	1.50	1.52	0.17	1.35	2.04	1.71	4.15	2.95	2.88	2.21	2.59	1.37	5.24	4.68
Pb	0.91	0.95	0.84	1.14	0.48	0.68	0.46	<0.30	<0.30	0.41	<0.30	0.42	1.19	<0.30	<0.30	<0.30	<0.30	0.33	<0.30	<0.30	0.85
Th	0.063	0.065	0.059	0.059	0.024	<0.014	<0.014	<0.014	<0.014	<0.014	<0.014	0.155	1.764	0.054	0.045	0.045	0.055	0.056	0.199	0.156	0.117
U	0.029	0.030	0.030	0.043	0.040	0.057	0.017	0.012	0.023	0.013	0.019	0.231	2.482	0.062	0.071	0.065	0.104	0.100	0.122	0.127	0.171
Mg no	89.4	89.4	88.9	88.7	87.4	83.5	86.6	90.4		90.3	90.6	88.5	89.4	89.4	89.6	90.0	89.9	89.7	89.9	90.0	89.1

	Folie Siffait		Blind international standards									LOD and LOQ for major and trace elements analyses					
	TGA126C	TGA127B	Blind UB-N					Blind JP-1				All samples					
wt.%							Ref. values					LOD	LOQ				
SiO_2	N.A	39.61			39.38		39.43					0.0834	0.1136				
TiO_2	N.A	0.017			0.09		0.11					0.0003	0.0006				
Al_2O_3	N.A	0.72			2.66		2.9					0.0088	0.0136				
FeO	N.A	8.54			8.44		8.34					0.0035	0.0041				
MnO	N.A	0.079			0.12		0.12			N.A		0.0001	0.0002				
MgO	N.A	38.02			35.99		35.21					0.0039	0.0092				
CaO	N.A	0.030			1.24		1.2					0.0064	0.0072				
Na_2O	N.A	<0.003			0.12		0.1					0.0020	0.0031				
K_2O	N.A	<0.014			0.02		0.02					0.0099	0.0143				
P_2O_5	N.A	<0.013			0.01		0.04					0.0088	0.0132				
LOI	N.A	13.52	RUNI	RUNII	RUNIII	Mean	Ref. values	RUNII	RUNIII	Mean	Ref. values	RUN I		RUN II		RUN III	
ppm												LOD	LOQ	LOD	LOQ	LOD	LOQ
Li	4.25	30.787	26.87	28.22	29.34	28.15	27	1.67	1.63	1.65	1.58	0.0306	0.0454	0.0875	0.1159	0.4628	0.5019
Be	<0.24	<0.247	N.A	N.A	N.A	-		N.A	N.A	-		0.0495	0.1190			0.1179	0.2475
Sc	12.9	8.891	12.79	12.63	10.27	11.90	13	7.57	9.22	8.40	7.34	0.4248	0.6896	0.1537	0.3013	0.2949	0.6007
V	46.3	20.584	64.11	61.74	61.56	62.47	63	22.8	25.7	24.3	24.9	0.1854	0.3749	0.0927	0.2112	0.0659	0.1427
Cr	2330	1063.968	3047.25	3216.28	2379.85	2881.13	2421	2140	2883	2511	2852	2.6772	5.3202	8.4427	9.9433	2.5966	5.3859
Co	105	114.936	101.04	104.48	104.17	103.23	102	117	117	117	121	0.1191	0.2496	0.1946	0.3544	0.1331	0.2780
Ni	2146	2579.720		2003.06	2013.97	2008.51	1942	2396	2383	2390	2474	N.A	N.A	0.4573	0.9628	0.7876	1.4793
Zn	43	39.750	82.83	67.57	78.98	76.46	84	40.6	52.0	46.3	46.7	1.2645	1.6313	19.4984	21.6635	1.5983	3.1820
Ga	1.70	0.657	2.66	2.48	2.53	2.55	3	0.546	0.633	0.589	0.467	0.3359	0.4039	0.0116	0.0202	0.0196	0.0289
Rb	0.35	0.397	3.41	3.82	3.29	3.51	3.32	0.243	0.314	0.278	0.288	0.0542	0.1153	0.1438	0.3076	0.0472	0.1092
Sr	3.10	2.837	6.66	7.27	7.43	7.12	7.7	0.628	0.601	0.615	0.546	0.0516	0.1025	0.0221	0.0596	0.0221	0.0587
Y	1.11	0.632	2.71	2.57	2.46	2.58	2.5	0.106	0.099	0.102	0.0823	0.0148	0.0402	0.0066	0.0195	0.0036	0.0112
Zr	0.91	1.488	4.32	3.40	3.38	3.70	3.8	5.8	5.9	5.9	5	0.1474	0.3058	0.0347	0.0854	0.0422	0.1084
Nb	0.21	0.316	0.06	0.06	0.04	0.05	0.06	0.041	0.055	0.048	0.0361	0.0174	0.0427	0.0024	0.0074	0.0083	0.0242
Cs	0.08	0.110	10.87	9.89	9.81	10.19	11.2	0.141	0.043	0.092	0.036	0.0012	0.0021	0.0020	0.0037	0.0019	0.0035
Ba	7.79	188.518	21.62	20.30	20.74	20.89	26.8	12.7	12.3	12.5	9.5	0.1598	0.4374	0.1815	0.4841	0.1170	0.3025
La	0.11	0.138	0.31	0.33	0.30	0.31	0.31	0.036	0.032	0.034	0.0268	0.0084	0.0228	0.0127	0.0335	0.0058	0.0166
Ce	0.13	0.223	0.88	0.78	0.79	0.82	0.83	0.068	0.053	0.060	0.0597	0.0178	0.0484	0.0176	0.0469	0.0109	0.0298
Pr	0.036	0.050	0.13	0.12	0.11	0.12	0.12	0.008	0.007	0.007	0.0074	0.0007	0.0013	0.0021	0.0041	0.0003	0.0006
Nd	0.12	0.163	0.62	0.60	0.62	0.61	0.62	0.041	0.030	0.036	0.0318	0.0325	0.0919	0.0312	0.0891	0.0255	0.0771
Sm	0.02	0.036	0.22	0.22	0.21	0.22	0.22	0.008	0.007	0.007	0.0084	0.0020	0.0046	0.0066	0.0115	0.0015	0.0033
Eu	0.015	0.034	0.08	0.08	0.08	0.08	0.08	0.002	0.003	0.003	0.0024	0.0007	0.0015	0.0010	0.0025	0.0007	0.0018
Gd	0.061	0.056	0.31	0.30	0.31	0.31	0.33	0.009	0.009	0.009	0.0097	0.0022	0.0046	0.0038	0.0083	0.0013	0.0029
Tb	0.019	0.015	0.06	0.06	0.06	0.06	0.06	0.002	0.002	0.002	0.0019	0.0005	0.0011	0.0014	0.0025	0.0003	0.0007
Dy	0.13	0.074	0.43	0.42	0.42	0.42	0.44	0.013	0.013	0.013	0.0146	0.0023	0.0051	0.0073	0.0131	0.0012	0.0029
Ho	0.038	0.020	0.10	0.09	0.10	0.10	0.1	0.003	0.003	0.003	0.0036	0.0005	0.0010	0.0012	0.0022	0.0003	0.0007
Er	0.117	0.052	0.28	0.28	0.28	0.28	0.29	0.012	0.012	0.012	0.0123	0.0015	0.0031	0.0019	0.0042	0.0006	0.0014
Yb	0.151	0.067	0.30	0.29	0.29	0.29	0.3	0.021	0.021	0.021	0.0209	0.0022	0.0045	0.0030	0.0063	0.0016	0.0032
Lu	0.026	0.013	0.05	0.04	0.05	0.05	0.05	0.005	0.004	0.004	0.0042	0.0004	0.0008	0.0005	0.0011	0.0004	0.0009
Hf	0.019	0.032	0.14	0.12	0.12	0.13	0.14	0.140	0.135	0.138	0.124	0.0053	0.0099	0.0013	0.0030	0.0026	0.0055
Ta	0.009	0.015	0.02	0.01	0.02	0.02	0.02	0.005	0.003	0.004	0.00304	0.0024	0.0043	0.0045	0.0068	0.0009	0.0018
W	0.14	2.423	15.37	15.64	21.43	17.48	19.9	1.030	0.734	0.882	0.8149	0.0071	0.0129	0.0099	0.0205	0.0127	0.0209
Pb	0.74	0.669	11.59	11.85	11.81	11.75	12.8	0.089	0.206	0.147	0.0765	0.0140	0.0190	0.0061	0.0092	0.2051	0.3009
Th	0.018	0.021	0.06	0.08	0.07	0.07	0.084	0.015	0.018	0.016	0.013	0.0027	0.0053	0.0067	0.0141	0.0028	0.0057
U	0.115	0.050	0.07	0.05	0.05	0.06	0.057	0.014	0.013	0.014	0.0123	0.0006	0.0014	0.0004	0.0009	0.0008	0.0019
Mg no		88.7															

RUN I : TGA009C, TGA018E, TGA126C, TGA127B, TGA136A, TGA138A, TGA140A, TGA140Ad; RUNII : TGA009A, TGA009B, TGA341A, TGA341E, TGA342A, TGA343A, TGA344A, TGA344B, TGA345A, TGA345B, TGA345C, TGA346B, TGA348E; RUNIII : TGA018J, TGA018K

LOD : Limit Of Detection; LOQ : Limite Of Quantification

Table 5

Click here to download Table: Table 5.docx

Table 5

In-situ La-ICPMS analysis of pargasite (ppm)

Locality	Pont de Barel						Ty Lan								
Sample name	TGA007C						TGA346A-102								
Analysis numb	TGA007C-101	TGA007C-102	TGA007C-103	TGA007C-104	TGA007C-105	TGA007C-106	TGA346A-101	TGA346A-102	TGA346A-103	TGA346A-104	TGA346A-105	TGA346A-106	TGA346A-107	TGA346A-108	TGA346A-109
Li	7.13	8.21	59.19	10.86	12.57	10.79	97.58	16.88	35.95	102.66	58.97	58.27	79.36	48.91	49.23
B	13.27	24.97	85.74	48.23	58.77	41.19	11.64	18.5	21.93	17.78	22.56	22.73	4.58	5.7	12.24
Ca	73655.12	72163.74	49501.99	60209.77	60296.47	64731.04	75927.86	62959.67	60210.96	71438.76	67833.02	58344.09	78612.14	81659.82	73079.06
Sc	81.35	73.65	73.74	67.8	72.9	82.49	89.01	55.55	84.61	69.91	75.05	65.41	33.04	53.45	48.45
Ti	4309.7	4185.7	4097.26	3789.76	3997.34	4433.55	1014.68	462.48	828.87	860.25	866.36	809.05	932.34	1041.33	1047.06
V	370.63	360.95	360.45	332.95	343.24	366.52	399.75	188.52	340.8	320.42	326.03	299.3	186.13	247.99	234.56
Cr	4630.7	4804.16	5562.91	4175.15	4255.08	4480.88	8942.65	4573.58	7643.53	8812.52	8740.42	8479.46	1116.17	4245.66	1569.55
Co	40.09	38.15	52.52	54.63	52.44	46.78	47.03	40.5	35.31	42.26	47.24	55.96	34.49	31.85	36.25
Ni	788.41	796.14	877.66	900.14	806.33	776.7	952.05	765.94	860.42	867.07	933.24	1004.1	943.23	864.45	919.84
Cu	4.65	2.33	3.19	3.33	3.1	3	3.3	3.67	4.54	2.62	3.66	4.04	2.19	2.69	3.32
Ga	4.3	4.37	4.04	4.22	3.97	3.85	6.12	2.82	4.49	6.24	5.36	5.12	9.25	8.54	8.23
Rb	3.13	3.38	2.66	2.66	2.92	2.91	9.71	2.78	5.78	8.17	6.68	6.76	6.35	7.84	6.91
Sr	189.68	188.32	133.39	152.04	151.77	160.66	433.92	162.07	323.52	388.2	344.3	303.38	400.72	383.86	365.33
Y	24.35	21.75	23.14	19.23	20.9	21.44	12.13	6.16	11.21	14.4	12.95	11.75	16.84	17.78	16.98
Zr	17.5	16.2	16.82	15.09	16.07	17.98	21.17	8.89	15.97	26.07	23.58	21.19	48.38	36.32	40.86
Nb	0.452	0.473	0.545	0.46	0.444	0.474	11.1	4.27	6.46	10.31	8.69	8.57	24.29	13.71	15.34
Mo	0.088	0.08	0.304	0.059	0.191	0.135	0.189	0.264	0.061	0.099	0.105	0.131	0.053	0.057	0.055
Sn	0.352	0.382	0.335	0.227	0.336	0.341	0.354	0.228	0.302	0.701	0.695	0.583	1.44	1.246	1.351
Sb	<0.046	0.092	0.072	0.056	0.13	0.285	0.668	0.566	0.262	0.328	0.225	0.246	0.578	0.297	0.296
Cs	0.364	0.384	0.423	0.547	0.595	0.558	0.0844	0.162	0.204	0.13	0.1216	0.0949	0.0993	0.1463	1.001
Ba	258.18	270.41	196.76	214.41	219.13	222.46	702.14	134.21	294.64	373.01	355.57	296.24	345.11	366.17	340.06
La	6.06	6.37	6.3	5.34	5.51	5.49	35.5	10.56	21.05	37.11	20.07	21.45	49.83	35.57	34.6
Ce	13.93	13.93	14.17	12.4	12.19	12.48	87.82	38.59	73.56	97.95	70.66	70.66	111.61	98.48	94.39
Pr	1.311	1.297	1.315	1.121	1.134	1.175	9.86	5.37	9.93	12.04	9.6	9.41	12.94	12.5	12.04
Nd	4.82	4.66	4.72	4.19	4.08	4.3	33.93	21.16	38.28	45.93	37.44	37.01	48.01	49.37	47.68
Sm	1.656	1.502	1.563	1.378	1.526	1.513	5.42	3.48	6.27	7.72	6.79	6.61	8.52	9.37	8.93
Eu	0.663	0.669	0.635	0.554	0.579	0.613	1.566	0.852	1.603	2.08	1.816	1.686	2.3	2.36	2.29
Gd	2.78	2.59	2.79	2.337	2.48	2.52	3.69	2.238	3.91	5.02	4.52	4.27	6.28	6.59	6.35
Tb	0.56	0.495	0.535	0.437	0.482	0.488	0.445	0.254	0.466	0.593	0.536	0.499	0.739	0.766	0.741
Dy	3.93	3.63	3.78	3.23	3.44	3.57	2.317	1.225	2.184	2.86	2.57	2.42	3.5	3.66	3.49
Ho	0.904	0.827	0.882	0.742	0.796	0.798	0.428	0.2175	0.4	0.497	0.463	0.421	0.577	0.632	0.618
Er	2.8	2.513	2.7	2.186	2.379	2.463	1.235	0.553	1.075	1.294	1.219	1.105	1.53	1.602	1.558
Tm	0.406	0.373	0.387	0.317	0.346	0.37	0.1827	0.0754	0.1517	0.1877	0.1634	0.147	0.202	0.213	0.213
Yb	2.81	2.588	2.75	2.311	2.485	2.543	1.211	0.582	1.07	1.264	1.14	1.085	1.351	1.477	1.377
Lu	0.409	0.383	0.404	0.334	0.358	0.369	0.1877	0.0828	0.1644	0.19	0.1785	0.1626	0.1977	0.215	0.2012
Hf	0.818	0.786	0.788	0.712	0.777	0.869	0.446	0.238	0.419	0.89	0.892	0.796	2.88	1.91	2.35
Ta	0.0251	0.0275	0.0351	0.0251	0.023	0.0238	0.31	0.1367	0.256	0.515	0.423	0.438	1.954	0.865	1.238
W	0.0227	0.0074	0.0212	0.0186	0.0118	0.0077	1.852	3.67	0.212	0.0525	0.0601	0.0924	0.0052	0.0055	0.464
Tl	0.0697	0.0498	0.0452	0.1099	0.0427	0.0435	0.285	0.0848	0.1544	0.215	0.173	0.17	0.193	0.187	0.178
Pb	4.64	4.61	4.34	3.76	3.92	4.2	18.38	6.26	10.95	17.3	12.43	12.47	15.32	13.8	12.6
Th	0.1578	0.232	0.357	0.232	0.25	0.137	4.46	0.334	0.582	1.701	0.584	1.306	2.98	0.62	10.91
U	0.0705	0.1139	0.2001	0.1166	0.1213	0.0501	1.529	0.0818	0.1835	0.296	0.1776	0.261	0.842	0.229	0.404

Concentrations calculated using Glitter softwareTM